ISSN 2312-1718

DUET JOURNAL

Volume 6, Issue 1, December 2020

Dhaka University of Engineering & Technology, Gazipur, Bangladesh

Editorial Board

Table of Contents

Synthesis and Characterization of PVA Based Anion Exchange Membranes for Solid Polymer Electrolytes

Khurshida Sharmin[1*] and Heshmat Aglan[2]

[1]Department of Mechanical Engineering, Dhaka University of Engineering & Technology, Gazipur, Bangladesh
[2]Tuskegee University, Alabama, USA

ABSTRACT

In this paper, a solid polymer electrolyte membrane based on poly vinyl alcohol (PVA) is formulated. The anion exchange membrane (AEM) is composed of dinonylnaphthaleindisulfunic acid and cross-linker triallylamine; while it is soaked in a potassium hydroxide (KOH) solution for 2h. Ionic conductivity was investigated with the variation of dinonylnaphthaleindisulfunic acid content and KOH concentration. The 15% acid modified membrane's conductivity reached 0.163 S/cm at room temperature while the neat membrane's conductivity was 10^{-3} S/cm. Though the mechanical testing revealed that with the increase of acid amount the modified membranes strength was decreased; however, the strength is sufficient to perform. The neat PVA membrane showed a Tg of about 84 °C, while the modified 15% acid membrane showed a Tg of 87 °C. Higher conductivities at room temperature, excellent thermal stabilities, and sufficient mechanical strength proved this AEM as a promising candidate for solid electrolyte fuel cell.

1. INTRODUCTION

The attention to polymer electrolyte membranes has been increasing continuously due to their potential use in electric vehicles, hydrogen sensors, electrochomic devices and fuel cells [1]. Because of global warming and a shortage of energy, fuel cell technology is an attractive alternative. Polymer electrolyte fuel cells emit no pollution and, in fact, produce water as a byproduct. A polymeric electrolyte membrane (PEM) replaces the traditional porous separator of batteries and resolves the problems that are caused by the use of a liquid phase electrolyte, such as internal shorting, leakage and the possibility of combustion at the surface of the electrode.

The polymer electrolyte membrane fuel cell (PEMFC) is popular due to its light weight, high power density and provision of continuous power [2]. There are two types of PEMs–a proton conducting membrane (PCM) and an anion exchange membrane (AEM). The PEMFCs exhibit some significant problems, the use of a PCM like Nafion suffers from the high methanol permeation and it needs a large amount of Pt catalyst to attain high power density [3,4]. In order to overcome these problems many works have been done to develop an efficient and better-performing membrane [5-8]. The AEM offered numerous advantages such as performance of electrode kinetics, ability of using non precious material as catalysts, and cost over the PCM [9]. In AEM, OH- anions are conducting instead of H+ though the membrane to provide current [3,5,8]. In alkali medium the oxygen reduction reaction occurs faster; here a non-precious material like silver or nickel can be used as a catalyst [10].

Wang et al. used a three step systemic method (chloromethylation, quarternization and alkalization) to prepare an AEM based on a poly-ether-imide [9]. This AEM had an ionic conductivity of 2.51×10^{-3} S/cm at room temperature. In chloromethylation, chloromethyl groups were added in order to load more hydroxyl ions in the polymer chain; during alkalization the OH^- anions were bonded to the polymer matrix by replacing the Cl^- ions. The effect of alkali concentration and temperature on the ionic conductivity was examined, achieving an ionic conductivity of 3.5×10^{-3}S/cm at 90 °C. The conductivity was approximately same at different KOH concentrations. The AEM system was improved by using a polysulfonade, where the ionic conductivity was studied with respect to temperature and amount of KOH concentration [8]. The highest number of chloromethyl groups were attained at 75 °C reaction temperature and 75 min reaction time and showed the maximum ionic conductivity of 7.33×10^{-2}S/cm.

Xiong et al. studied a PVA AEM for a fuel cell in an easier method than the thee step method [7]. PVA was grafted with trimethylammonium chloride groups by quarternization and then cross linked with gluteraldehyde (GA). The

*Corresponding author's email: ksharmin1130@duet.ac.bd

membrane showed anionic conductivity of 7.34×10^{-3}S/cm and improved the methanol properties compared to the Nafion 117 membrane. The quarternized polymer electrolyte is unstable in an alkaline environment above 60 ^{o}C [11]. To further investigate this, Qiao et al. prepared a new cost effective cross linked alkaline PVA membrane with GA for high chemical stability [3]. However, the higher concentration of KOH (4.0M) saturated the PVA matrix and made it too viscous for ion mobility. Hence the membranes were soaked in higher concentration of KOH, resulting in membranes with the ionic conductivities at 6.0M and 10.0M KOH of 8.47×10^{-4}S/cm and 9.77×10^{-4}S/cm, respectively. The absorbing capacity, i.e. the charge carrier concentration of PVA membrane, was increased and hence the ionic conductivity was increased. Qiao et al. modified the AEM membrane by blending the PVA with poly vinyl pyrolidone (PVP) and following the same procedure [11]. The 1:0.5 mass ratio of PVA/PVP showed the maximum ionic conductivity of 0.53 S/cm soaked in KOH prior to measure. The membrane was highly stable at higher temperature120 ^{o}C. The same high ionic conductivity was measured soaking in KOH for poly-acrylic acid (PAA) mixed with PVA and cross linked by triallylamine [6]. Increasing the amount of PAA resulted in an increase in ionic conductivity for the 24h KOH soaked membrane. A higher amount of OH^- ions can be rationalized to diffuse into PVA chain due to soaking in KOH solution for a longer time. In another study, Shang et al. demonstrated a PVA grafted with bis-crown ether monomer. It resulted with a higher conductivity of 0.235 S/cm at 80 °C comparing the other existing PVA membranes and alkaline stability [12].

In a study, a highly durable long side-chain polybenzimidazole (PBI) AEM (N-PBIs) were fabricated successfully; where the OH- conductivity of N-PBI membrane achieved 0.11 S/cm at 80 °C [13]. Another work based on imidazolium, AEMs showed conductivity up to 1.0×10^{-2} S/cm at 90 °C [14]. The ionic conductivity of most of the AEMs were measured in contact of water or doped in KOH solution prior to measurement and showed conductivity in the range of 10^{-3}-10^{-1} S/cm [3,7,10,11,15]. Results from some other research groups showed a conductivity of 10^{-1} S/cm and 10^{-2} S/cm at higher temperature [13-14, 16].

In previous studies the highest conductivity is found in the range of 10^{-1} S/cm which is measured at high temperature and soaked for longer time. Most of the reported membranes are soaked in alkaline solution for long time before measurement. To eliminate this longer time soaking, a cross-linked anion exchange membrane based on PVA is fabricated here. The PVA solution with dinonylnaphthaleindisulfonic acid and a cross linker, triallylamine, is casted in a Teflon mold. The cross linker interacts with the hydroxyl group of PVA and builds up a crosslink structure. The fabricated membrane is soaked in KOH solution for 2h; and found stable in this alkaline environment. Ionic conductivity of the membrane is measured at room temperature (not soaked in water during measurement); at dry condition after doping in KOH solution. At room temperature this PVA solid electrolyte membrane showed a conductivity of 10^{-1} S/cm. Tensile and thermal properties of the membranes are also investigated.

2. EXPERIMENTAL PROCEDURE

2.1 Materials

Poly-vinyl-alcohol, dinonylnaphthalenedisulfonic acid, triallylamine and potassium hydroxide solution were used to fabricate anion exchange membrane. Poly-vinyl-alcohol (99+% hydrolyzed, molecular weight 89000-98000) in powder form was supplied by Sigma Aldrich. Dinonylnaphthalenedisulfonic acid was obtained from Sigma Aldrich as a deep brown viscous solution. The solvents were isobutanol (55 wt.%) and 2-methyl-1-propanol (45 wt.%). Liquid Triallylamine was used as cross linking agent and was provided by Sigma Aldrich. Potassium hydroxide (KOH, 56.11 gm/mol.) was obtained from Sigma Aldrich in white pellet form.

2.2 Fabrication of AEM

The neat PVA membrane was prepared by a simple solution casting method. PVA powder was mixed with distilled water at 90 °C for 20 minutes to make a 10wt.% solution. The solution is viscous and transparent after complete dissolution in water. This solution was poured onto a Teflon mold and dried at room temperature. When dry, the membranes were peeled out from the mold. The average thickness of the neat membranes was about 0.15-0.25 mm.

PVA anion conductive membranes were prepared by adding dinonylnaphthalenedisulfonic acid (wt./wt.) to the neat PVA 10 wt% solution. The PVA/acid mixture was stirred mechanically on a magnetic stirrer until a homogeneous solution was obtained. By varying the amount of acid, membranes of different acid concentrations (5 wt.%, 15 wt.%, 20 wt.%) were prepared. A 60 wt.%

of KOH and 3 wt.% of cross linker triallylamine based on wt.% of PVA were dissolved in distilled water. The KOH-cross linker solution was mixed with the homogeneous PVA/acid solution and stirred at 60 °C for about 2h until a homogeneous and clear solution was obtained. This solution was cast on a Teflon mold and then dried at room temperature. The average thickness of the modified membranes was about 0.60-0.75 mm.

The PVA membranes were soaked in an 8.0M KOH aqueous solutions for alkalization at room temperature and equilibrated for 2h. In this process KOH is doped into the PVA membrane [11]. Membranes were removed from the KOH solution, wiped and then dried at room temperature before conductivity measurement. Fig. 1 presents a block diagram describing the formulation procedure for the PVA anion exchange membrane.

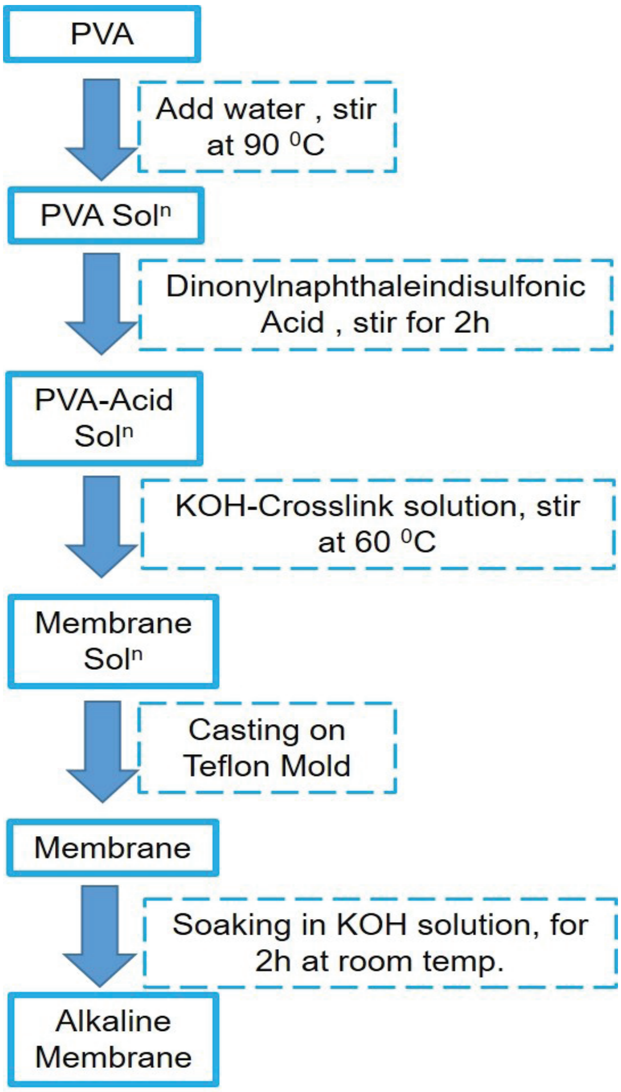

Fig. 1. Schematic diagram of preparation of PVA ion conductive membrane.

2.3 Characterization

Conductivity test: The anion conductivity of the membranes was calculated by the electrochemical impedance spectroscopy (EIS) method. The measurements were done using a PARSTAT 2273 (Princeton Applied Research Co., Power Suite Software) impedance analyzer in potentiostatic mode. The conductivity experiments were done at a frequency range of 10 Hz to 1.5 MHz; thirty points were collected within this frequency range. The electrode surface area was 2.51 cm^2. The resistance value was measured at the high frequency intercept of the impedance with the real axis. If the high frequency point didn't cut the real axis, the point was extrapolated to cut the real axis. The proton conductivity was calculated by using equation 1,

$$\sigma = t / (A \times R) \qquad (1)$$

where σ represent the conductivity of the membrane (S/cm), R is the measured resistance on the membranes (Ω), t is the thickness of membranes (cm) and A is the cross-sectional area (cm^2) perpendicular to current flow. The membranes were cut in small pieces and clamped between two copper electrodes. Five samples from each membrane were tested and the average value was taken as the conductivity of the membrane.

Fourier transform infrared (FTIR) spectroscopy: FTIR spectra were obtained using a Thermo-Scientific Nicolet 6700 FTIR Spectrometer with Smart Orbit diamond attenuated total reflectance (ATR) accessory. IR spectra were obtained at a resolution of 4.0 cm^{-1} over a 400 to 4000 cm^{-1} wave number range and 32 scans.

Differential scanning calorimetry (DSC): TA Instruments DSC Q1000 was used for the thermal scans of the membranes in the presence of nitrogen. The PVA modified membranes were subjected to a heat/cool/heat cycle to remove any thermal history that existed. The DSC thermograms for the samples that are shown in this study are the result of the second heating of the samples. For the PVA samples the heat cycle was ramped from room temperature to 250 °C at 10 °C/min and the cooling cycle followed at a speed of 15 °C/min from 250 °C to room temperature.

Thermogravimetric analysis (TGA): Thermal gravimetric analysis (TGA) was performed using a TA Instruments TGA Q500. Measurements were run under nitrogen, using a scan rate of 10 °C min^{-1}. The PVA samples were heated to 700 °C.

Tensile test: Tensile tests were conducted on the neat, and modified PVA membranes with a 44.5 N load cell. The

samples were cut into dog bones according to ISO 527-2-5A. The thickness of the samples was measured using a thin membrane thickness gauge (Timetrade TT 260). Five samples from each membrane were tested and the average value was taken as the ultimate strength. The samples were tested at a crosshead speed of 2.54 mm/min.

3. RESULTS AND DISCUSSION

3.1 Effect of Acid Amount on Ionic Conductivity

Fig. 2 shows the ionic conductivity of the PVA anion membranes as a function of acid concentration. The acid concentration was varied from 5% to 20% based on PVA wt.%. All modified membranes were dried after soaking in KOH solution. The highest ionic conductivity value of 0.163 S/cm was obtained by the 15% acid modified PVA membrane soaking at 8.0M KOH solution. Other two modified membranes also showed ionic conductivity of approximately 10^{-1} S/cm. The acid interpenetrated into the PVA matrix and resulted more charge carriers.

In this work, the fabricated PVA membranes showed 10 times higher conductivity compared to these established PVA membranes at room temperature [17-19]. The studies with established PVA anion exchange membranes found conductivity in the range of 10^{-2} S/cm at room condition. Shang et al. found a conductivity in the range of 10^{-1} S/cm at 80 ^{0}C; however, at room condition conductivity showed in the range of 10^{-2} S/cm [20].

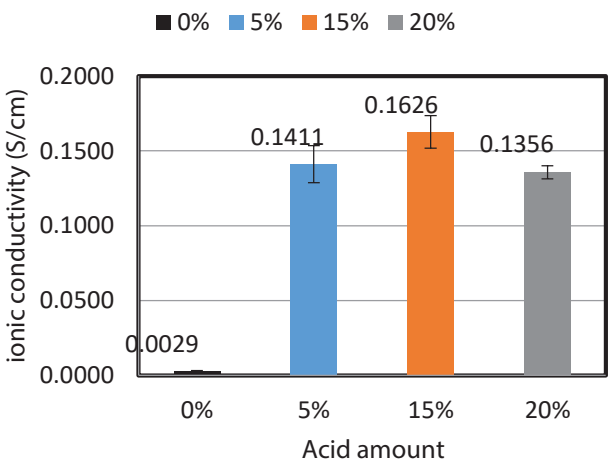

Fig. 2. Ionic conductivity of PVA membranes as a function of acid amount.

The Nyquist plots (electrochemical spectra) for the modified PVA membranes are shown in Fig. 3. All the samples showed half semi-circle Nyquist plots. The high frequency intercept part (squared part shown in Fig. 3) is shown in Fig. 4 in a larger form to describe the membrane's resistance. From the intercept point to the 'X' axis, resistance value can be read. The 15% acid membrane showed a minimum membrane resistance of 0.19 Ω, while 5% and 20% showed higher resistance value; which verify the ionic conductivity results in Fig. 2.

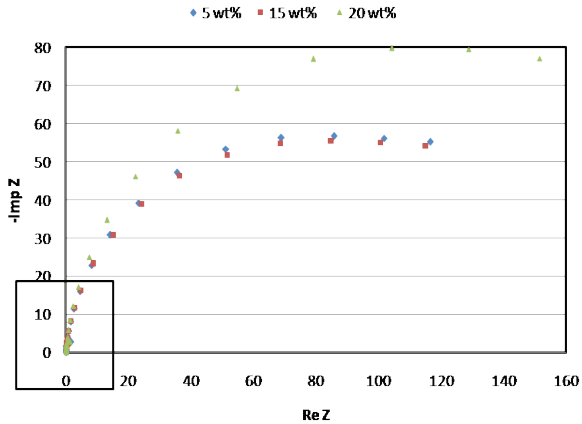

Fig. 3. Electrochemical spectra for PVA modified membranes.

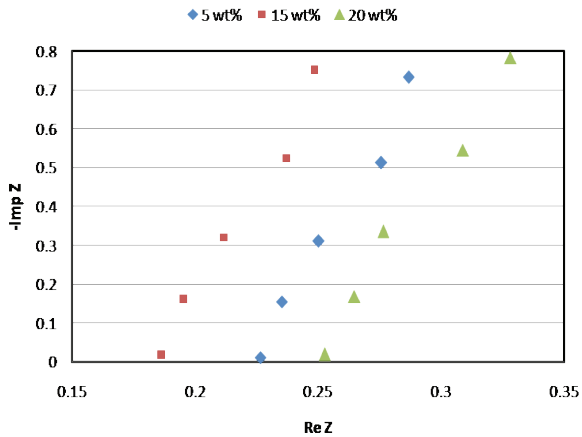

Fig. 4: Intercept part of Nyquist plot.

3.2 Effect of KOH Concentration on Ionic Conductivity

To Investigate the ionic conductivity at different KOH concentrations, the 15% acid membrane was chosen because of its higher ionic conductivity. The ionic conductivity measurements for different KOH concentrations are shown in Fig. 5. The conductivities were measured at 1.0M, 4.0M, 8.0M and 10.0M KOH concentrations at room temperature. The conductivity is increased with the increasing concentration of KOH

up to 8.0M concentration. Higher concentrations of KOH resulted in greater impregnation of OH- into the composite membrane. This doping of KOH also enhanced the percentage of water in the polymer matrix [4]. Water binds to KOH on the membrane, which indicates a stable swelling behavior. Higher conductivity proves the higher uptake of hydrophilic groups in the polymer matrix. In a study the swelling ratio of PVA: PAA sample showed three times more than that of pure PVA polymer membrane due to the uptake of the hydrophilic groups in the PVA/PAA polymer membrane system [6].

However, 10.0M KOH concentration did not contribute more to the ionic conductivity. The higher concentration of KOH limited the movement of the free ions in polymer chain, referred to as weak ionic mobility [3, 11].

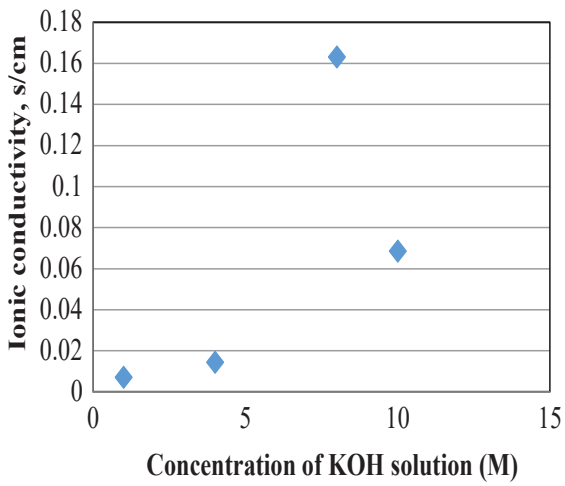

Fig. 5: Effect of KOH concentration on ionic conductivity of 15% PVA acid membrane.

3.3 FTIR STUDY

Fig. 6 shows the IR spectrum for neat PVA, 5% PVA acid and 15% PVA acid membranes. The characteristic peaks of neat PVA included 3252.0 cm^{-1} (-OH stretching vibration), 2936.5 cm^{-1} (C-H asymmetric stretching vibration), 1654 cm^{-1} (-OH symmetric wagging vibration), 1414 cm^{-1}, 1321 and 1085 cm^{-1} (C-H asymmetric and symmetric wagging vibrations) [21-22]. Compared with the spectrum of neat PVA, the relative intensity of the peaks around 3252 cm^{-1} and 2936 cm^{-1} decreased with the acid amount. This indicated possible interactions between the PVA polymer segment and the acid. The peaks at 1414 cm^{-1} and 1321 cm^{-1} for the acid containing membranes shifted closer and merged as one peak for 15% acid membrane. A new peak in the acid containing membranes at 1032 cm^{-1} was assigned to the -SO_3H group [23].

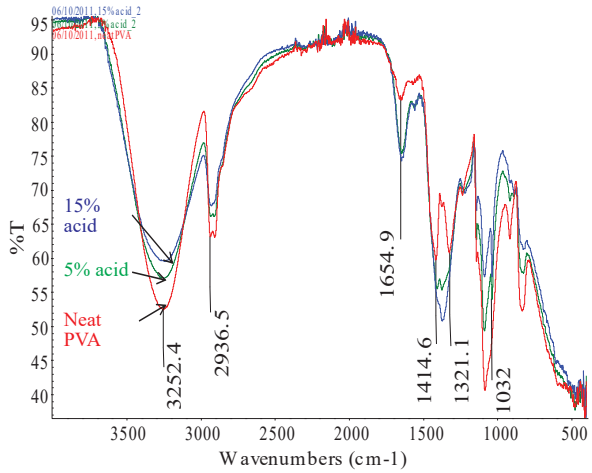

Fig. 6. FTIR spectra for neat PVA, 5% acid and 15% acid membranes.

3.4. Thermo-gravimetric (TGA) Analysis

Fig. 7 shows the TGA thermograms for neat PVA and acid containing modified PVA membranes. All the samples started to lose weight before 100 °C. The weight loss in the region between 80-150 °C was associated with the removal of water molecules from the polymer. After 150 °C, the neat PVA membrane showed a thermally stable region up to 240 °C. At 267 °C a 50% weight loss was observed due to the degradation of hydroxide groups on the polymer matrix [10-11]. The modified membranes showed a 35% weight loss at 180-200 °C region and 50% loss at 228 °C. The first loss at 35% was due to the decomposition of sulfonic acid groups [24] and the second loss at 50% was due to the decomposition of hydroxide groups. All the samples showed a weight loss in the 400-500 °C region due to the decomposition of main chain of PVA [11, 24]. In Fig. 7, it can be seen that the modified membranes contained higher residues at 680 °C than the neat membrane.

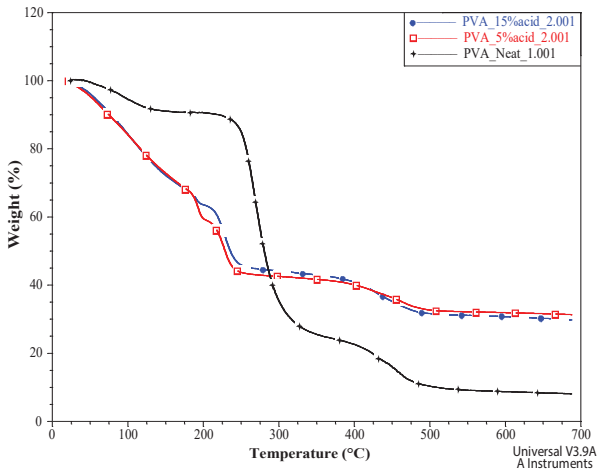

Fig. 7. TGA curves for neat PVA and acid containing PVA membranes.

3.5. DSC Analysis

Fig. 8 shows the second DSC thermal scans for the neat PVA and the 15% acid membranes. The glass transition temperature, T_g, of the neat PVA was 84.35 ˚ C. The 15% acid membrane showed a T_g of 87.89 ˚ C. Here the glass transition temperature is not changed significantly for the modified membrane in comparison to the neat membrane. In the first heating cycle the peak between 100 °C to 150 °C (not shown here) was due to removal of solvent water from the membranes. The melting of the neat membrane started at 210 ˚C and completely melted at around 228 ˚C. The degradation temperature of the acid membrane was 228 ˚C; this membrane was heated up to 210 ˚C. The melting peak of the acid membrane was not as clear as that for the neat membrane. However, it can be seen that the melting started at 200 ˚C for the acid membrane.

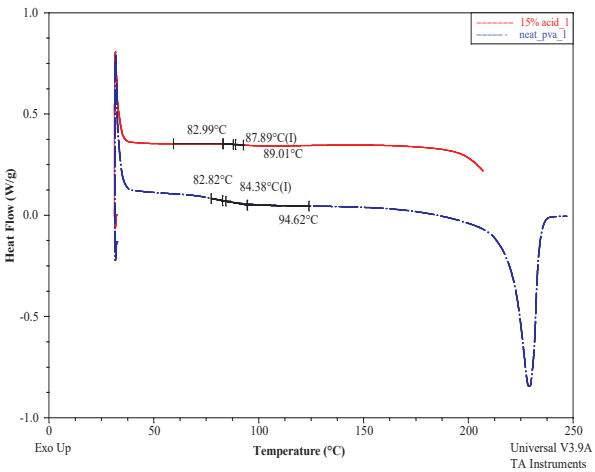

Fig. 8. Thermal scans for neat PVA and 15% acid containing membranes.

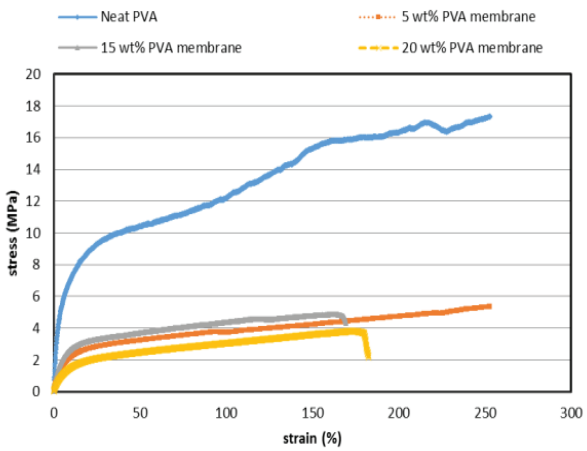

Fig. 9. Mechanical behavior of modified PVA and neat PVA membranes.

The strength of neat PVA membrane was about 16.9 MPa similar to that reported by Chen et al. [25]. The 5% acid membrane displayed a mechanical strength of 5.23 MPa and the elongation at break was 235.33%. The 15wt.% and 20wt.% membranes showed strengths of 4.91 MPa and 3.91 MPa, respectively. The strength and strain decreased with acid content. In thermal analysis it can be seen that the melting of PVA was reduced when the acid was added to the PVA polymer. It indicated the amorphous phase was increased [26] and the ionic conductivity was also localized to the amorphous region [27]. It was assumed that acid amount penetrated the PVA matrix and made it more amorphous. Table I summarizes the stresses and strains of the tested membranes. These strengths were better compared to the strengths of the PVA/poly-acrylic-acid membranes [6].

Table I: Stress-strain data for neat and modified PVA membranes

	Average Ultimate Tensile Strength (MPa)	Average Strain (%)
Neat PVA	16.9 ± 0.4	252.33 ± 14.2
5 wt.% acid	5.23 ± 0.29	235.33 ± 30.59
15 wt.% acid	4.91 ± 0.08	194.67 ± 25.93
20 wt.% acid	3.91 ± 0.18	168.14 ± 19.14

4. CONCLUSION

In this paper, a PVA based AEM with high conductivity are synthesized and evaluated the tensile and thermal performance of the membranes. The membranes are fabricated by casting method while dinonylnaphthaleindisulfonic acid and a cross linker, triallylamine, are used. Three different modified membranes are studied here – 5%, 15% and 20% based on wt.% of acid content. The PVA polymeric membrane showed excellent film-forming ability and an excellent OH− conductivity with alkaline stability. The 15% acid modified membrane showed the highest anion conductivity of 0.163 S/cm (10^{-1} S/cm) at room temperature while the neat membrane's conductivity was 10^{-3} S/cm. The strength of the acid modified membrane revealed that increasing the acid amount reduced the strength of the membrane. The 5% acid membrane showed higher strength compared to 15% and 20% acid membranes. Thermal analysis of 15% acid membrane has shown that the Tg was 87 °C, which was higher than that of the neat PVA membrane (84 °C Overall, higher conductivity and thermomechanical properties proved the 15% acid modified membrane as a strong and reliable candidate for solid electrolyte membrane.

ACKNOWLEDGEMENT

We thank the Raytheon Company, USA for the financial support.

REFERENCES

[1] W. Li, M. Yuan, and M. Yang, "Dual-phase Polymer Electrolyte with Enhanced Phase Compatibility based on Poly(MMA-g-PVC)/PMMA," European Polymer Journal, Vol. 42, pp. 1396–1402, 2006.

[2] S. Ahmad, S. Ahmad, and S. A. Agnihotry, "Nanocomposite Electrolytes with Fumed Silica in Poly(methylmethacrylate): Thermal, Rheological and Conductivity Studies" Journal of Power Sources, Vol. 140, pp. 151–156, 2005.

[3] J. Qiao, J. Fu, X. Wang, J. Ma, and T. Okada, "Alkali Doped Poly(vinyl alcohol) for Potential Fuel Cell Applications," Synthetic Metals, Vol. 160, pp. 193-199, 2010.

[4] S. J. Lue, W. T. Wang, K. P. O. Mahesh, and C. C. Yang, "Enhanced Performance of a Direct Methanol Alkaline Fuel Cell (DMAFC) using a Polyvinyle Alcohol/Fumed Silica/KOH Electrolyte," Journal of Power Sources, Vol. 195, pp. 7991-7999, 2010.

[5] J. S. Park, S. H. Park, S. D. Yim, Y. G. Yoon, W. Y. Lee, and C. S. Kim, "Performance of Solid Alkaline Fuel Cells Employing Anion-Exchange Membranes," Journal of Power Sources, Vol.178, pp. 620–626, 2008.

[6] G. M. Wu, S. J. Lin, and C. C. Yang, "Preparation and Characterization of PVA/PAA Membranes for Solid Polymer Electrolytes," Journal of Membrane Science, Vol. 275, pp. 127-133, 2006.

[7] Y. Xiong, J. Fang, Q. H. Zeng, and Q. L. Liu, "Preparation and Characterization of Cross-Linked Quarternized Poly Vinyl Alcohol Membranes for Anion Exchange Membrane Fuel Cells," Journal of Membrane Science, Vol. 311, pp. 319-325, 2008.

[8] G. Wang, Y. Weng, D. Chu, R. Chen, and D. Xie, "Developing a Polysulfone-Based Alkaline Anion Exchange Membrane for Improved Ionic Conductivity," Journal of Membrane Science, Vol. 332, pp. 63-68, 2009.

[9] G. Wang, Y. Weng, D. Chu, D. Xie, and R. Chen, "Preparation of Alkaline Anion Exchange Membranes Based on Functional Poly(Ether-Imide) Polymers for Potential Fuel Cell Applications," Journal of Membrane Science, Vol. 326, pp.4-8, 2009.

[10] Y. Xiong, Q. L. Liu, Q. G. Zhang, and A. M. Zhu, "Synthesis and Characterization of Cross-Linked QuaternizedPoly Vinyl Alcohol/Chitosan Composite Anion Exchange Membranes for Fuel Cells," Journal of Power Sources, Vol. 183, pp. 447-453, 2008.

[11] J. Qiao, J. Fu, R. Lin, J. Ma, and L. Liu, "Alkaline Solid Polymer Electrolyte Membranes Based on Structurally Modified PVA/PVP with Improved Alkali Stability," Polymer, Vol. 51, pp.4850-4859, 2010.

[12] D. J. Kim, B.-N. Lee, and S. Y. Nam, "Synthesis and Characterization of PEEK Containing Imidazole for Anion Exchange Membrane Fuel Cell," International Journal of Hydrogen Energy, Vol. 42, pp. 23759-23767, 2017.

[13] S. Li, X. Zhu, D. Liu, and F. Sun, "A Highly Durable Long Side-Chain Polybenzimidazole Anion Exchange Membrane for AEMFC," Journal of Membrane Science, Vol. 546, pp. 15-21, 2018.

[14] B. Lin, G. Qiao, F. Chu, J. Wang, T. Feng, N. Yuan, S. Zhang, X. Zhang, and J. Ding, "Preparation and Characterization of Imidazolium-Based Membranes for Anion Exchange Membrane Fuel Cell Applications," International Journal of Hydrogen Energy, Vol. 42, pp. 6988-6996, 2017.

[15] T. Feng, B. Lin, S. Zhang, N. Yuan, F. Chu, M. A. Hickner, C. Wang, L. Zhu, and J. Ding, "Imidazolium-Based Organic–Inorganic Hybrid Anion Exchange Membranes for Fuel Cell Applications," Journal of Membrane Science, Vol. 508, pp. 7-14, 2016.

[16] C. X. Lin, Y. Z. Zhuo, E. N. Hu, Q. G. Zhang, A. M. Zhu, and Q. L. Liu, "Crosslinked Side-Chain-Type Anion Exchange Membranes with Enhanced Conductivity and Dimensional Stability," Journal of Membrane Science, Vol. 539, pp. 24-33, 2017.

[17] X. Du, Z. Wang, H.Zhang, W. Liu, Z. Chen, J. Xu, "Double network anion exchange membrane with excellent flexibility and stability." Journal of Membrane Science, Vol. 587, 117178, 2019.

[18] Z. Yang, M. Zhang, Y. Xiao, X. Zhang, and M. Fan, "Facile Fabrication of Poly(vinyl alcohol)/ Polyquaternium-10 (PVA/PQ-10) Anion Exchange Membrane with Semi-Interpenetrating Network." Macromol. Mater. Eng., 2000506 (1-12), 2020.

[19] A. Muhamad Samsudin and V. Hacker, "Preparation and Characterization of PVA/PDDA/Nano-Zirconia Composite Anion Exchange Membranes for Fuel Cells." Polymers, 11, 1399, 2019.

[20] C. Shang, Z. Wang, L. Wang, J. Wang, "Preparation and characterization of a polyvinyl alcohol grafted bis-crown ether anion exchange membrane with high conductivity and strong alkali stability." International Journal of Hydrogen Energy, 2020.

[21] L. Zhang, "Synthesis and Characterization of Novel Proton-Conductive Composite Membranes Derived from the Hybridization of Metal Oxyhydroxide Nanoparticles and Organic Polymers for Fuel Cell Applications," MS Thesis, Duke University, USA, 2010.

[22] J. Li, J. Suo, and L. Jia, "Morphologies and Mechanical Properties of Organic–Inorganic Multilayered Composites," Polymer Engineering Science, Vol. 50, pp. 689-696, 2010.

[23] J.W. Lee, J.H. Kim, N.S. Goo, J.Y. Lee, and Y.T. Yoo, "Ion-Conductive Poly Vinyl Alcohol-Based IPMCs," Journal of Bionical Engineering, Vol. 7, pp. 19-28, 2010.

[24] D. S. Kim, I. C. Park, H. II. Cho, D. H. Kim, G. Y. Moon, H. K. Lee, and J. W. Rhim, "Effect of Organo Clay Content on Proton Conductivity and Methanol Transport though Crosslinked PVA Hybrid Membrane for Direct Methanol Fuel Cell," Journal of Industrial and Engineering Chemistry, Vol. 15, pp. 265-269, 2009.

[25] W. Chen, X. Tao, P. Xue, and X. Cheng, "Enhanced Mechanical Properties and Morphological Characterizations of Poly(vinyl alcohol)-Carbon Nanotube Composite Films," Applied Surface Science, Vol. 252, pp.1404-1409, 2005.

[26] C. C. Wang, "Study of Alkaline Nanocomposite Polymer Electrolytes Based on PVA–ZrO2–KOH," Material Science & Engineering B, Vol. 131, pp. 256-262, 2006.

[27] C. C. Wang, and S.J. Lin, "Preparation of Composite Alkaline Polymer Electrolyte," Material Letters, Vol. 57, pp. 873-881, 2002.

Microstructure Analysis of Microbial Concrete: A Comparative Study

Sudipto Nath Priyom, Md. Fahad Shahriar Zawad, Md. Asifur Rahman* and Md. Moinul Islam

Department of Civil Engineering, Chittagong University of Engineering & Technology, Chattogram, Bangladesh

ABSTRACT

This paper represents a critical comparison between conventional concrete and concrete developed using "Bacillus cereus" and "Escherichia coli" (E. coli) bacterial culture to determine the effect of the genus Bacillus and non-Bacillus bacteria on concrete microstructure. The durability and uniformity performance of concrete specimens were evaluated through Ultrasonic Pulse Velocity (UPV) test and Water Absorption Capacity (WAC) test for different curing ages. Scanning Electron Microscopy (SEM) analysis was conducted to visualize the Microbial Calcite Precipitation of bacterial concrete. UPV and WAC tests showed that concrete specimens containing bacterial culture possess more density and uniformity than the conventional one. SEM analysis established the presence of bacterial impressions and calcite layer inside the concrete, which contributed to the improvement of impermeable characteristics of concrete. Concrete specimens containing "Bacillus cereus" showed better performance than "E. coli" in all aspects.

1. INTRODUCTION

Being one of the most used materials worldwide, the assessment in the context of the durability of the concrete is now a significant challenge for Civil Engineers. The techniques of having concrete of variable strengths are very available nowadays. But the methods of keeping them durable for year after year are not so many.

The role of the concrete is to bear the compressive or tensile loads and these generally lead to the crack development inside the concrete. The freeze-thaw actions, shrinkage may however, also be the reason behind crack development. Although this generally does not affect concrete significantly in terms of strength, the cracks created can be worked as the pathway to the waters, harmful foreign matters and chemical solutions (sulfates, acids, chlorides). This eventually spoils the homogeneity of the concrete matrix inside and degrades the quality of the rebar embedded, which leads to the corrosion later volume expansion and development of major crack inside the concrete. From the past decade, various eco-friendly approaches are taken to make the concrete more durable and uniform. In this regard, microstructure development and increment of impermeable capacity are taking a significant part.

The incorporation of bacteria inside the concrete as a self-healing agent as well as an agent to develop the mechanical and microstructure properties have been introduced by the researchers recently. The calcite-precipitating bacteria can be introduced to the concrete mix directly as a solution or also can be incorporated as a form of immobilized object [1-3]. The microbial precipitation greatly depends on the type of bacteria as well as the type of nutrients that has been used in the solution [4].

Therefore, the selection of the culture medium and bacteria is very important for this technique. Apart from this, the whole microbial process of self-healing by calcite precipitation inside the concrete varies in terms of some conditions like: pH, Calcium concentration, dissolved inorganic Carbon concentration, nucleation sites, etc. [5]. The technique provides long-term durability of concrete by introducing easy crack repairing way and reduces the cost of structural maintenance to a great extent. The use of bacterial culture to develop inner properties of concrete is also becoming more popular as it is totally eco-friendly and the result found is also very attractive. Incorporation of bacteria inside the concrete can decrease the water absorption capacity of concrete by about 60%-70% than the conventional concrete [6].

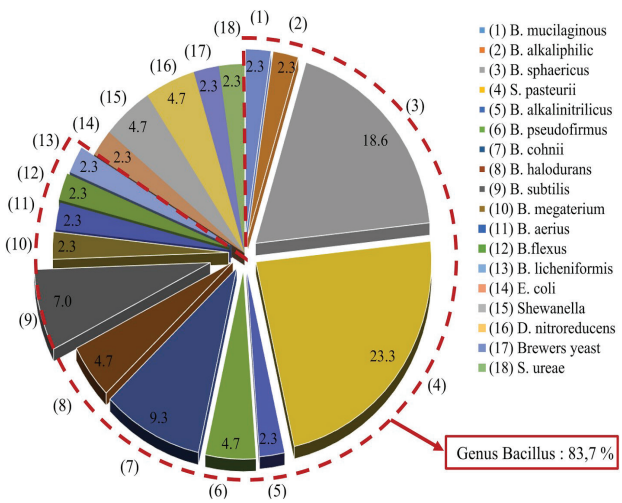

Fig. 1: Different types of bacterial usage in concrete [7]

*Corresponding author's email: asifurmahin752@gmail.com

Several bacteria have been used by the researcher in this regard and most of which has given positive result in terms of durability assessment. But, in this specific context genus Bacillus has the highest rate of usage in this regard (about 84%) [Fig. 1]. Fig. 1 actually shows the application of different bacteria in cementitious material over the periods. For this experimental investigation, Bacillus cereus bacteria was chosen from genus Bacillus and Escherichia coli *(*E. coli*)* from non-Bacillus genus. The major target of this experiment is to observe the effect of bacterial culture in concrete microstructure properties through Ultrasonic Pulse Velocity (UPV), Water Absorption Capacity (WAC) and Scanning Electron Microscopy (SEM) analysis approach and to compare the effect of the genus Bacillus and non-Bacillus genus in concrete microstructure.

In this durability assessment investigation after the successful incorporation of Bacillus cereus and E. coli bacterial culture inside the concrete several curing period (days) was completed. Ultrasonic Pulse Velocity test, Scanning Electron Microscopy analysis and Water Absorption Capacity test was conducted to analyze and compare the relative resistivity and durability of different samples having different contents of bacteria.

The ultrasonic pulse velocity (UPV) test is the widely used non-destructive test used to determine the quality and structural integrity of concrete after construction. An ultrasonic pulse is allowed to pass through the cast sample and the velocity of the pulse is determined. The denser and higher the integrity of the inner matrix of the concrete, the more durable will be the concrete. The cylindrical specimens having diameter of 100 mm and height of 200 mm was used in this test. The UPV test generally provides improved and more accurate result with the aging of concrete. Rather than testing at 28 days curing period, if prolonged cured samples than this can be tested the more reliable result can be found [8]. So, UPV test was conducted on the specimens for 60 days and 200 days of curing age. The Water Absorption Capacity (WAC) test result resembles the development of resistivity to water penetration and also gives a good indication about the inner microstructure of the concrete specimen. To analyze the reduction of the porosity, Water Absorption Capacity test was conducted at 200 days curing age. Scanning Electron Microscopy (SEM) analysis was also conducted on the prepared samples in order to see the actual image of the concrete sample composed of the desired ingredients on micro-scale and from this analysis, the void presents and the dispersion of various constituents inside the sample can easily be determined. From this respected analysis, the microscopic images of the microstructure of concrete specimens were observed and the effect of bacterial culture and their relative comparison were made.

This environment-friendly and bio-chemical concrete is the most efficient one among all for making the structure durable. This technique can reduce the maintenance cost of construction by lessening the frequent expensive repairing works.

2. EXPERIMENTAL PROGRAM

2.1 Preparation of Bacterial Culture

Bacillus cereus and E. coli, both facultative anaerobic, spore-forming, rod-shaped bacterium which is easily accessible from the environment, were selected as the bacterial agent for this experimental investigation. Both of the bacteria were selected due to their carbonate precipitation capacity. “Bacillus cereus,” a representative from genus Bacillus, was selected for the comparison with “E. coli,” a representative of genus Escherichia. Both of the bacteria are easily accessible from nature. So the cost-effective approach was also one of the vital points for selecting those respective bacteria. Rather than depending on cell count technique, optical density was chosen to control the cell concentration of the bacteria in the culture.

An optical density of 0.5±0.1 was chosen in this form of study depending on the previous result found in the optimum optical density investigation. LB media mechanism was chosen for the growth and maintenance of both bacterial strains. Autoclaving and seeding process was maintained according to the prescribed rules. Flow diagram of detailed experimental program is represented by Fig. 2. The prepared bacterial cultures used in concrete mixing are shown in Fig. 3 and Fig. 4.

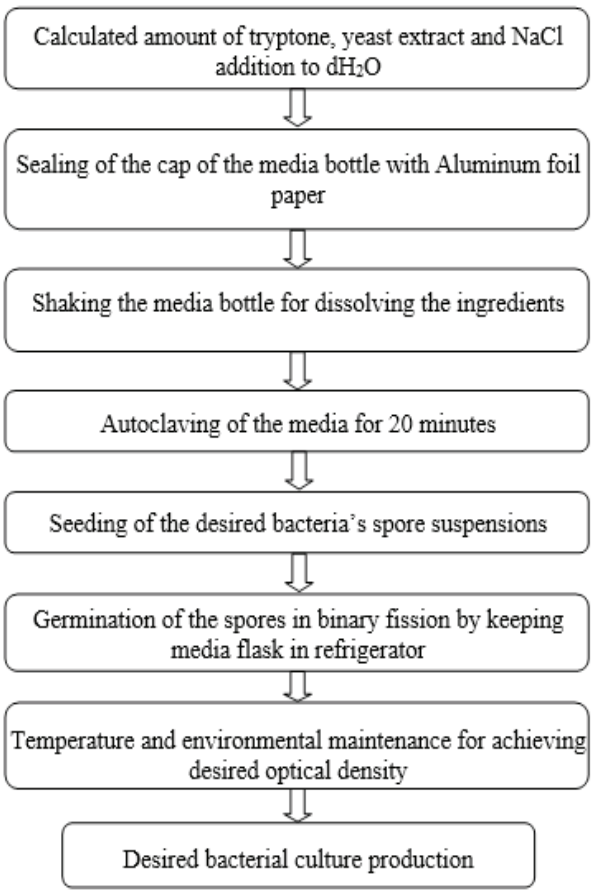

Fig. 2: Process followed for bacterial culture preparation

Fig. 3: Bacillus cereus bacterial culture

Fig. 4: E. coli bacterial culture

2.2 Mix Proportions, Specimen Details and Material Properties

Concrete specimens were prepared according to ACI standard procedure. Three different mixtures with Portland Composite Cement (PCC) (CEM II) were done with design strength of 20 MPa. Mix ratio was derived as 1.0:2.57:2.72. Cylindrical concrete specimens of 100 mm diameter and 200 mm high were cast for all respective tests.

Locally available sand was used as fine aggregate. The coarse aggregate was 12.5 mm nominal size crushed stone. Table 1 and Table 2 report the properties of aggregates used in this experimental investigation.

Table 1: Properties of Fine Aggregate

Fineness Modulus	2.53
Specific Gravity	2.62
Absorption Capacity	2.76%
Water Content	6.81%

Table 2: Properties of Coarse Aggregate

Unit Weight	1581.4 kg/m^3
Specific Gravity	2.76
Absorption Capacity	2.31%
Water Content	5.96%

Bacillus cereus and E. coli enriched bacterial cultures were prepared having optical density (OD_{600}) 0.5±0.1. The bacterial cultures were added directly to the concrete mix after achieving desired growth stage and optical density.

Bacterial culture was added as a full replacement of water required for mix design. Concrete specimens with and without bacterial culture were cured in tap water following ASTM C1602 guidelines.

For UPV test all the specimens were cured for 60 and 200 days in order to observe the long-term effect of bacteria inside the concrete. For SEM analysis longer curing specimens were taken. Intermediate curing and testing weren't done in order to check the behavior of bacteria induced concrete for 60 and 200 days curing effect. In this experimental investigation, the major target was to see the impact of bacterial culture in concrete properties in the case of long-term. Being cured for 60 and 200 days, the specimens were kept in open air under laboratory conditions. The temperature was maintained in between 25 – 27 ºC. Table 3 represents the specifications of the specimens.

Table 3: Specimen specifications

Specimens	Bacterial concentration (%)	Bacterial agent
M-1	0	None
M-2	100	Bacillus cereus
M-3	100	E. coli

3. TESTING LAYOUT

This study investigated the effects of bacteria in concrete due to long term curing. Three different types of concrete specimens were prepared with and without microbial water.

For each test, three specimens of every group were tested and the average of them was taken as the result.

3.1 Ultrasonic Pulse Velocity (UPV) Test

UPV test can evaluate the inner quality of concrete specimens. It can assess whether the inner core of the concrete specimen is dense and uniform or if there is void. UPV test was done on cylindrical specimens by placing a pulse transmitter on one face of the cylinder and a receiver on the opposite side. A timing machine was used to find out the results. Table 4 shows the chart to categorized specimens depending on UPV results. Depending on this chart, the tested specimens were categorized according to their results.

Table 4: Quality grading of concrete

Pulse Velocity (km/sec)	Concrete Grading
Above 4.5	Excellent
3.5-4.5	Good
3.0-3.5	Medium
Below 3.0	Poor/Doubtful

3.2 Scanning Electron Microscopy (SEM) Analysis

SEM analysis was conducted for following two major targets.

- To compare the micro-structural difference between conventional concrete and bacterial concrete; and
- To observe and compare micro-structural differences between Bacillus cereus and E. coli induced concrete

For SEM analysis, powdered samples were collected from the core of each specimen. SEM analysis was conducted according to the standard procedure. In SEM analysis, Interfacial Transition Zone (ITZ) was focused specially to visualize the bacterial mineral deposition, which produces a filler effect in the cement-sand matrix. Fig. 5 represents the SEM analysis machine that was used to conduct the respective analysis.

Fig. 5: SEM analysis machine used for this study (Model: JSM 7600F, JEOL-JAPAN)

3.3 Water Absorption Capacity (WAC) Test

Water absorption capacities of cylindrical specimens were evaluated for 60 and 200 days of curing periods. It was done to observe the effect of bacteria on concrete permeability during long run. The test was conducted according to ASTM C642 standard. To perform the test, the specimens were initially taken out from the curing environment and they were weighed during their SSD condition (W_0). Then the specimens were placed in to an oven at 100°C for 24 hours and the mass of the dry condition (W_1) was taken. Following equation was used to find out the result.

$$\text{Water absorption (\%)} = [(W_0 - W_1) / W_1] \times 100 \quad (1)$$

4. TEST RESULTS AND DISCUSSION

4.1 Ultrasonic Pulse Velocity (UPV)

UPV test was conducted on concrete specimens having 0% bacterial culture, 100% Bacillus cereus enriched microbial culture and 100% E. coli enriched microbial culture with curing ages of 60 and 200 days. In the case of the UPV result, higher pulse velocity represents higher uniformity and density of the specimens. UPV test was conducted with a large gap between two curing ages in order to observe the effect of bacteria at long run. It was done to ensure whether any negative changes occur during long curing period. Table 5 and 6 represent the results of the UPV test and the categorization of concrete specimens depending on it.

Table 5: UPV results and categorization of specimens (60 days curing age)

Group	Pulse Velocity (km/s)	Concrete Grading
M-1	3.50	Good
M-2	3.63	Good
M-3	3.58	Good

Table 6: UPV results and categorization of specimens (200 days curing age)

Group	Pulse Velocity (km/s)	Concrete Grading
M-1	3.67	Good
M-2	3.89	Good
M-3	3.78	Good

For M-2 and M-3 mixes, the UPV results were much higher than the conventional one for both curing ages. For M-2 mix, the result was the highest one. It may be due to the usage of bacterial culture of "Bacillus cereus" which has the ability of more $CaCO_3$ precipitation inside concrete. The pores between cement-sand matrices were filled up by the addition of bacterial culture. Apart from M-2, a better result was also found in M-3 mix. M-3 mix possesses E. coli bacterial culture.

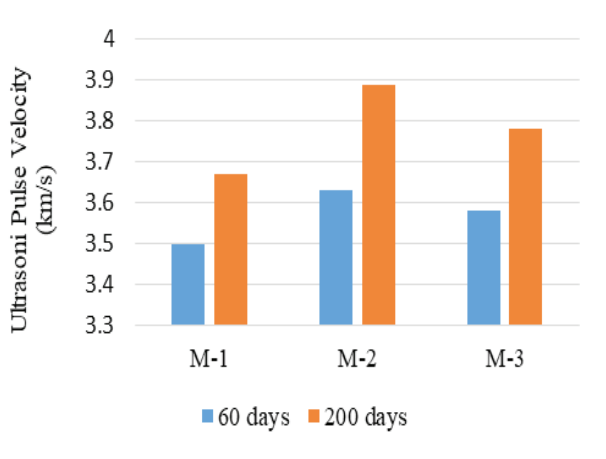

Fig. 6: Comparison between UPV results through bar chart

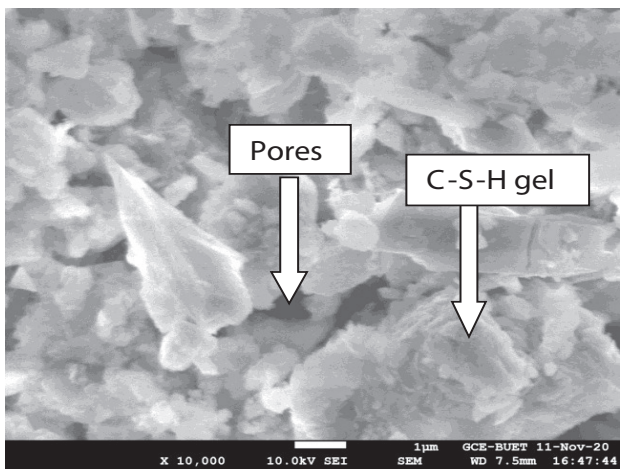

(a)

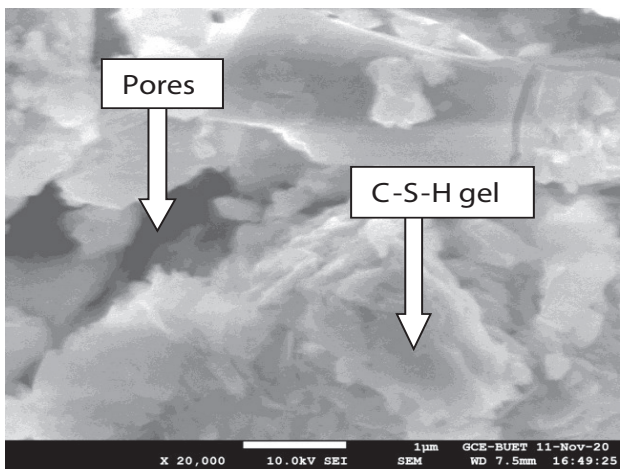

(b)

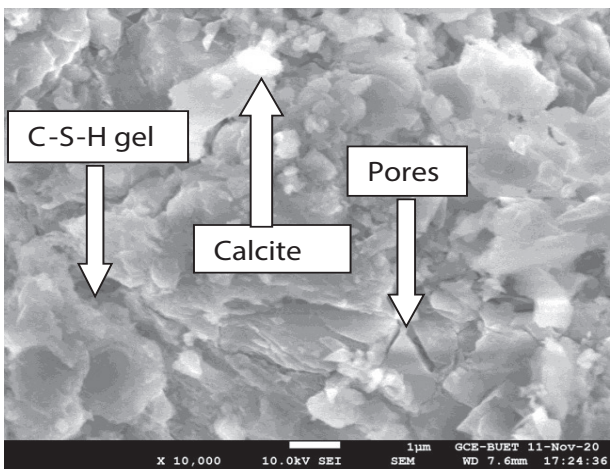

(c)

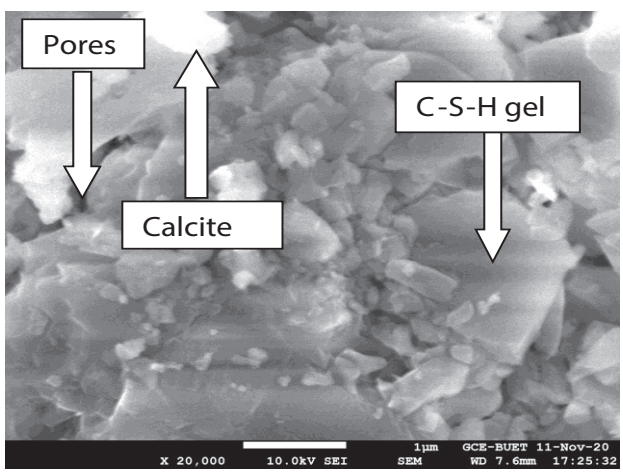

(d)

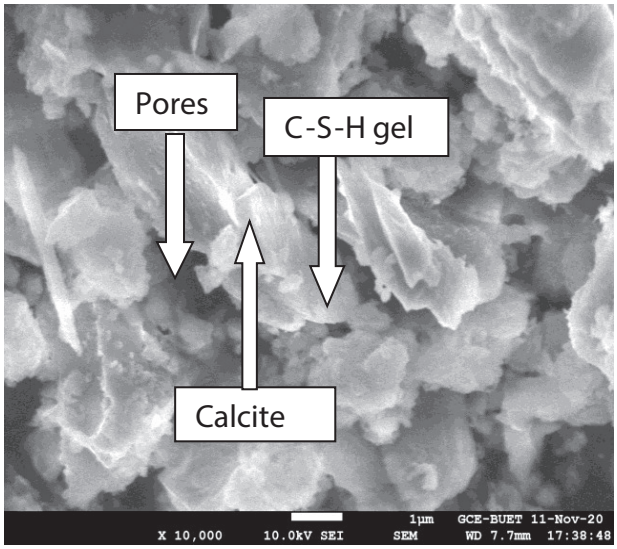

(e)

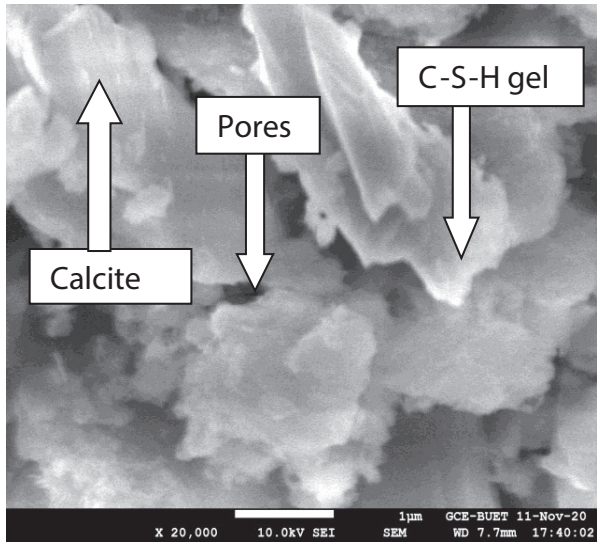

(f)

Fig. 7: SEM images of (a) M-1 (X 10000); (b) M-1 (X 20000); (c) M-2 (X 10000); (d) M-2 (X 20000); (e) M-3 (X 10000); (f) M-3 (X 20000)

Figure 6 graphically represents all the results obtained from the UPV test. As compared to the conventional one, both bacteria-induced concretes have given better results. The microbial carbonate precipitation in the concrete matrix is the main reason behind it. This kind of precipitation technique acts as a filler element that dense the microstructure of concrete. UPV test results strongly indicate this phenomenon. From SEM analysis, this phenomenon can be ensured. It can be seen that for both curing ages, M-2 concrete has given better results than M-3.

4.2 SEM Analysis

Figure 7 shows the scanning electron microscopic images of the samples, which comprises the microscopic images at a preferable magnification range and from these images, the relative comparison among these three types of concrete mixes (M-1, M-2 and M-3) can be carried out. Each of the samples was tested in powdered form.

Figure 7(a) and 7(b) show the formation of calcium silicate hydrate or C-S-H gel. For 0% bacterial culture, the CSH gel is relatively dispersed and less compacted. The formation of portlandite $Ca(OH)_2$ and calcite can also be observed in the samples. From these images, pores in microstructure can also be observed.

Sample incorporating Bacillus cereus has shown the best result foremost. Figure 7(c) and 7(d) show that the structural compactness and densification which are foremost maximum in this investigation among the other comparative elements. The C-S-H gel is well dispersed and the precipitation of the calcite crystal causes effective strength gain. The pores are at a minimum level, which can be counted as negligible.

M-3 mix in Figure 7(e) and 7(f) exhibit a better result than that of the control one. Here the structure shows relatively better compactness and denser formation. It shows better effective strength than M-1 mix due to this structural formation. This increased strength is because of the calcite production by the bacteria E. coli.

Among all concrete mixes, M-2 and M-3 possess contrasting textures. Being the conventional one, M-1 shows minimum crystal growth whereas the crystalline matrix can be seen in M-2 and M-3 mixes. So as compared to the conventional one, the samples having bacterial culture showed more developed microstructure.

Now, in between M-2 and M-3 mixes, SEM images of M-2 mix are looking denser, and the pores are lesser than M-3 mix. Concentrations of relatively large crystals can be seen in M-2 mix. The textural setting of M-2 mix resembles that coherence between particles of sand and the microstructural matrix is probably enhanced due to crystallization at the concrete matrix. Though the microstructure of M-3 mix is also promising but micro-structural analysis of M-2 mix shows denser and durable characteristics.

The analysis shows that concrete having bacterial constituent demonstrates better result in term of strength and compactness of the structure, which leads to the durability and sustainability of the structure in harsh conditions. Moreover, the comparison between the bacterial concretes exhibits that the concrete having Bacillus cereus has the better comparative preference to concrete having E. coli.

4.3 Water Absorption Capacity (WAC)

Water absorption capacity of concrete resembles its porous and permeable characteristics. Higher value in this regard represents more permeable structure. Increase of permeability decreases the concrete's durability. Table 7 and 8 represent the water absorption capacity values of concrete specimens at 200 days curing age. Long curing day was taken to observe the microbial carbonate precipitation of bacterial concrete samples.

Table 7: WAC results of specimens (60 days curing age)

Group	Water Absorption Capacity (%)
M-1	5.23
M-2	2.87
M-3	3.12

Table 8: WAC results of specimens (200 days curing age)

Group	Water Absorption Capacity (%)
M-1	4.51
M-2	1.91
M-3	2.08

From Table 7 and 8, it can be seen that with respect to M-1 mix, the water absorption capacities of M-2 and M-3 mixes decrease a lot. It is due to the use of bacterial culture which has the ability to reduce the pores in concrete matrix.

In between two microbial groups, M-2 concrete's absorption capacity is about 8-10% less than M-3. This explains that Bacillus cereus bacterial culture has a greater ability to precipitate carbonate in concrete microstructure which can be the main reason behind it. So, between M-2 and M-3 group, M-2 group shows the most promising result in the case of absorption capacity.

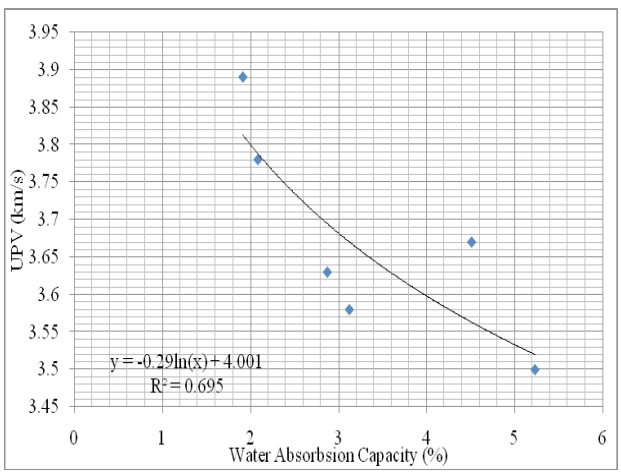

Fig. 8: Relationship between WAC (%) and UPV (km/s)

Later on, a relationship between water absorption capacity and UPV was developed. The graph in Fig. 8 resembles a parabolic shape from which it can be seen that for higher UPV value, the absorption capacity is lower. The correlation formula is found as,

$$Y = -0.29\ln(x) + 4.001$$

$$R^2 = 0.695$$

The regression value indicates an acceptable relationship between WAC and UPV data. It indicates that 69.5% data of the regression model fits actual observations.

5. CONCLUSION

This research was conducted to investigate the effect of bacterial culture on concrete microstructure through non-destructive tests and to compare the results. In this investigation, two different genus bacteria were taken as bio-agents in order to investigate their suitability and differences through the analysis of concrete microstructure. It was done in order to find out the most effective genus through a comparative study. A long gap between curing days was taken to observe the micro-structural changes more accurately. The obtained results from the investigation highlight the following conclusions:

1. Bacterial concrete incorporating E. coli and Bacillus cereus individually has higher pulse velocity than the conventional concrete, which provides comparatively better uniformity, densification and effective strength gain.
2. Concrete having Bacillus cereus demonstrates relatively higher pulse velocity than the one having E. coli, which proves the comparative betterment of the first one in terms of compactness and less porousness.
3. SEM image analysis shows comparatively densified and compacted inner structure of the bacterial concrete than the conventional concrete.
4. Having a relatively higher dispersion of CSH gel in microstructure, concrete incorporating Bacillus cereus may possess higher effective strength gain than the E coli incorporated one.
5. Concrete samples having bacterial culture possess lower permeability and water absorption capacity than conventional concrete.
6. Comparison between Bacillus cereus and E. coli showed that Bacillus cereus incorporated concrete absorbs less water and possess more compact microstructure.

7. A relationship between UPV and WAC has been developed which may be helpful in developing durable concrete.
8. Due to the high compactness and integrity of the inner structure of the specimens as found from test results, Microbial concrete is recommended to be a wise solution for making concrete durable, and the use of Bacillus cereus can be a better option in this case.

ACKNOWLEDGEMENT

The authors declared no conflict of interest. The authors would like to gratefully acknowledge the support and services provided by the department of Civil Engineering, Chittagong University of Engineering and Technology (CUET) and Bangladesh University of Engineering and Technology (BUET) for their laboratory facilities in order to complete this research project. The authors also expressed their deep gratitude to all the staffs of Department of Microbiology, University of Chittagong, for providing all kinds of technical facilities.

REFERENCES

[1] P. Ghosh, S. Mandal, B. D. Chattopadhyay and S. Pal, "Use of microorganism to improve the strength of cement mortar," Cement Concr. Res., 35 (10), pp 1980–1983, 2005.

[2] J. June, U. Politecnica, J. Y. Wang, K. Van Tittelboom, N. De Belie and W. Verstraete, "Potential of applying bacteria to heal cracks in concrete," in: J. Zachar, P. Claisse, T. R. Naik, E. Ganjian (Eds.), Proceedings of the International Conference on Sustainable Construction Materials and Technologies June 28-June 30, Università Politecnica delle Marche, Ancona, Italy, 978-1-4507-1490-7, pp. 1807–1818, 2010.

[3] H. Chen, C. Qian, and H. Huang, "Self-healing cementitious materials based on bacteria and nutrients immobilized respectively," Constr. Build. Mater., 126, pp 297–303, 2016.

[4] G. Mörsdorf and H. Kaltwasser, "Ammonium assimilation in Proteus vulgaris, Bacillus pasteurii, and Sporosarcina ureae," Arch. Microbiol, 152 (2), pp 125–131, 1989.

[5] F. Hammes and W. Verstraete, "Key roles of pH and calcium metabolism in microbial carbonate precipitation," Rev. Environ. Sci. Biotechnol., 1 (1), pp 3–7, 2002.

[6] S. S. Raina, E. S. Singla, and V. S. Batra, "Comparative analysis of compressive strength and water absorption in bacterial concrete," International Journal of Engineering Development and Research (IJEDR), 6(3):281-286, ISSN: 2321-9939, 2018.

[7] T. H. Nguyen, E. Ghorbel, H. Fares and A. Cousture, "Bacterial self-healing of concrete and durability assessment," Cement and Concrete Composites, Volume 104, 103340, ISSN 0958-9465, 2019.

[8] T. Gehlot, S. S. Sankhla, S. S. Gehlot, and A. Gupta, "Study of Concrete Quality Assessment of Structural Elements Using Ultrasonic Pulse Velocity Test," IOSR Journal of Mechanical and Civil Engineering. 13. 15-22. 10.9790/1684-1305071522, 2016.

[9] N. De Belie, "Application of bacteria in concrete: a critical evaluation of the current status," RILEM Technical Letters, (1), pp 56–61, 2016.

[10] K. Vijay, M. Murmu, and S. Deo, "Bacteria based self healing concrete – A review," Construction and Building Materials152:1008-1014, 2017.

[11] J. Xu, and W. Yao "Multiscale mechanical quantification of self-healing concrete incorporating non-ureolytic bacteria-based healing agent," Cement and concrete research, Vol. 64, pp. 1-10, 2014.

[12] F. Inagaki, Y. Motomura, and S. Ogata "Microbial silica deposition in geothermal hot water," Appl Microbiol Biotechnol; 60(6):605–12, 2003.

Impact of Air Bubble Entrainment of Breaking Waves on Radiation Stress

Md. Nur Hossain[1*], Md. Ashabul Hoque[2], Md. Motiur Rahman[1], Most. Nasrin Akhter[1] and Md. Masudar Rahman[3]

[1]Department of Mathematics, Dhaka University of Engineering & Technology, Gazipur, Bangladesh

[2]Department of Mathematics, University of Rajshahi, Bangladesh

[3]Department of Mathematics, Bangladesh Army University of Engineering and Technology, Natore, Bangladesh

ABSTRACT

The current investigation is engaged with the discussion of radiation stress on allowing air bubble entrainment by breaking waves on an inclining sea shore in the surf zone. Beside of this, a vertical velocity component term has also been calculated letting air bubble effect, theoretically. To calculated wave set-up, the momentum balance equation has been modified by developing radiation stress term. Finally, the equation has been solved by using the Lax-Wendroff method of a progressive wave. It has been also checked a stability analysis for this method. The results demonstrate a good agreement with the experimental data and some popular model which is presented in the text.

1. INTRODUCTION

When waves propagate to the close shore zone, wave profiles turn out to be steeper and subsequent waves break. As a result, the air bubble entrainment is occurred into the breaking waves (Fig. 1). Breaking waves on beaches induce variations in radiation stress, driving longshore currents.

Radiation stress is the motion of energy, which is conveyed by the sea waves. At the point when these waves break, that energy is moved to the water segment, constraining nearshore flows [9]. Generally, the radiation stress assumed a significant function in different oceanographic wonder. For the clarification of different seaside confounded marvel, the radiation stress is required, particularly in breaking waves. For base bathymetric impacts in the close to shore the waves in the end steepen and breaks in the surf zone. At the point when wave is breaking, a thick tufts of air pockets makes and disseminates energy and force. Our comprehension of the breaking cycle itself is restricted, notwithstanding, to the absence of estimation.

Several researchers [6, 8, 10, 16] studied the surf zone hydrodynamics, but didn't incorporate air bubble for the breaking waves phenomenon. For random breaking waves, wave height and wave setup are calculated by [17]. Radiation stress and set-up in the near-shore region are calculated by [7], but breaking complexity is not included. A portion of the early attempts to contemplate the air bubble entrainment in the breaking waves in the surf zone

Fig. 1: Entrainment of air bubble in the breaking waves on a sloping beach.

are studied by [4]. At introductory stages, the entrained air bubble are answerable for dispersing the wave energy detailed in [18]. The reason for an abrupt decrease of wave stature and wave energy inside the surf zone could be entrained air rises into water guaranteed by [15]. A hypothetical investigation of the air bubble entrainment under the wind wave breaking in the sea surface layer had been summed up by [11]. An air bubble model proposed by [19] considering air bubble changes with water depth exponentially and checked by a series of laboratory data. Interaction of air and water and corresponding distribution

*Corresponding author's email: nurbpj14@gmail.com

is examined in the surf zone by [12]. As in [5] the storm wave height distribution is calculated, but the contribution of air bubble is neglecting. A dissipation model proposed by [3], taking air bubble effect linearly various with water depth but does not incorporate radiation stress for calculating wave set up in the surf zone.

For solving a system of nonlinear differential equation in hyperbolic or parabolic geometry numerically, [1,20] discussed the Lax-Wendroff scheme for better accuracy. Wave height and wave setup are calculated numerically by forward finite difference model which was found in [2, 18]. Linear water waves problems are solved by the Lax-Wendroff scheme that was described in [14].

Albeit various researchers have created various models dependent on various plans to figure out wave set-up in the surf zone, but still no one is included radiation stress considering air bubble effect. The present study concerns about this direction.

In this paper, the discussion is centered around developing radiation stress considering air bubble impact straightly fluctuates with water depth in the surf zone. Also, the vertical velocity component is calculated considering air bubble effect. Vertical velocity term can be used for better understanding of breaking waves in two dimensional study. The introduced plan incorporates void portion appropriations, air volume, modified vertical velocity component, radiation stress and momentum balance equation for computing wave setup. The wave set up of spilling and plunging breaking waves have processed in the surf zone by dissecting hypothesis and information. Finally, the results have been compared with the numerical and the experimental data.

2. MATHEMATICAL FORMULATION

2.1 Basic Assumption

Since [13] recommended that the void fraction dispersion fluctuates exponentially with water depth in the surf zone, yet from the perception of genuine field, void fraction circulation is likewise conceivable to consider that it changes straightly with water depth as in [3].

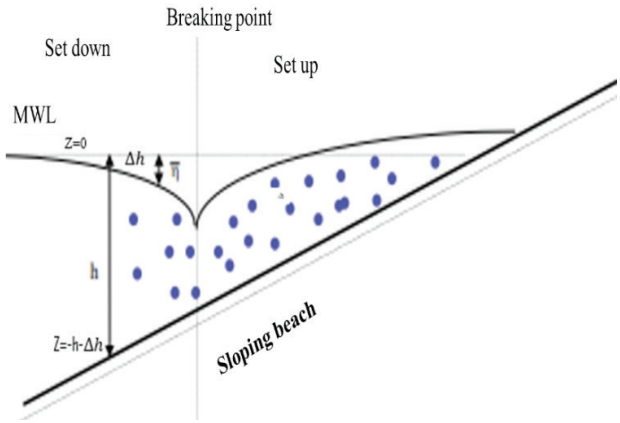

Fig. 2: Sketch of air bubble entrainment for breaking waves in the sloping beach.

The distribution of void fraction has been considered linearly varies with water depth (Fig. 2). The air bubble dispersion in the vertical way is given by the accompanying direct structure:

$$C(z) = \left(\frac{h + \Delta h + z}{h + \Delta h}\right) C_0 \qquad (1)$$

where is the proportion of the volume locally involved via air bubble per unit width, h is the still water depth and C_0 indicates the reference concentration at the mean water surface $z = 0$.

The following boundary conditions are satisfied:

i) $C(z) = C_0$ at the mean water surface z = 0

& ii) $C(z) = 0$ at z = - h

2.2 Volume of Air

The ascent of the free-surface level Δh is an element of the measure of entrained air and water depth. The overall volume of entrained air into water per unit width is characterized as:

$$\Delta h = \int_{-h-\Delta h}^{0} C(z)dz \qquad (2)$$

where z is letting vertically from the raised water surface. So that, from Eq. (2), we have

$$\Delta h = \frac{C_0 h}{2 - C_0} \qquad (3)$$

which is the volume of the entrained air in the breaking water wave in the surf zone.

2.3 Modified Vertical Velocity Component Term

For the reason of air entrained in the water of the surf zone corresponding vertical component term *w* is changing. So that, we need to compute *w* for the case of air entrained in the water.

It is well known that the continuity equation for steady and compressible flow is,

$$\nabla.(\rho\vec{V}) = 0 \tag{4}$$

$$\Rightarrow \frac{\partial}{\partial x}(\rho u) + \frac{\partial}{\partial z}(\rho w) = 0 \tag{5}$$

But, for the reason of air entrained in the water, we have

$$\left.\begin{aligned} u &= u_w \\ w &= w_w + w' \\ p &= p_w \\ \rho &= (1-C)\rho_w \end{aligned}\right\} \tag{6}$$

where, *w* denote the water and w' denote the correction term, ρ is the function of *z* only of the system. Using these values in the above equation and simplified, we get

$$\frac{\partial w'}{\partial z} - \frac{(w_w + w')}{(1-C)}\frac{C_0}{h+\Delta h} = 0 \tag{7}$$

with the help of Eq. (1),

$$\frac{\partial w'}{\partial z} + \frac{w'}{z+(h+\Delta h)(1-1/C_0)} = -\frac{w_w}{z+(h+\Delta h)(1-1/C_0)} \tag{8}$$

Integrating Factor of Eq. (8) is given by,

$$e^{\int \frac{1}{z+(h+\Delta h)(1-1/C_0)}}$$

Multiplying Eq. (8) by integrating factor, we obtain

$$w'\{z+(h+\Delta h)(1-1/C_0)\} = -\int w_w dz$$

$$= -\frac{\pi H}{T\sinh(kh)}\sin(\omega t - kx)\int \sinh k(h+z)dz \tag{9}$$

where, $w_w = -\frac{\pi H \sinh k(h+z)}{T\sinh(kh)}\sin(\omega t - kx)$

$$= -\frac{\pi H}{T\sinh(kh)}\sin(\omega t - kx)\frac{\cosh k(h+z)}{k} + c' \tag{10}$$

where, c' is the integrating constant.

Now, with the help of Eq. (1), we get

$$c' = -\frac{\pi H}{T\sinh(kh)}\sin(\omega t - kx)\frac{\cosh k(\Delta h)}{k}$$

Finally, we get

$$w' = \frac{p}{k}\left[\frac{\cosh k(\Delta h)}{z+(h+\Delta h)(1-1/C_0)} - \frac{\cosh k(h+z)}{z+(h+\Delta h)(1-1/C_0)}\right] \tag{11}$$

where,

$$p = \frac{\pi H}{T\sinh(kh)}\sin(\omega t - kx) \tag{12}$$

Therefore, the vertical velocity component is

$$w = \frac{\pi H \sin(\omega t - kx)}{T\sinh(kh)}\left[\sinh(h+z) - \frac{1}{k\{z+(h+\Delta h)(1-1/C_0)\}}\{\cosh k(h+z) - \cosh k(\Delta h)\}\right] \tag{13}$$

2.4 Radiation Stress Considering Air Bubble Effect

Radiation stress is the overabundance stream of energy because of essence of the waves announced by [9]. The transition of force is included by two commitments: one because of wave – actuated speeds of the water particles and another because of the pressing factor. Presenting the air bubble impacts, the time found the middle value of radiation stress toward wave engendering is characterized as the time arrived at the midpoint of complete energy motion because of the presence of waves short the mean transition without waves which is written as:

$$S'_{xx} = \overline{\int_{-h-\Delta h}^{\bar{\eta}} (p+\rho u^2)dz} - \int_{-h-\Delta h}^{0} (p_0 - \rho g\Delta h)dz \tag{14}$$

After simplification, we obtain

$$S'_{xx} = \overline{\int_{-h-\Delta h}^{\bar{\eta}} pdz} + \overline{\int_{0}^{\bar{\eta}} pdz} + \overline{\int_{-h-\Delta h}^{\bar{\eta}} \rho u^2 dz} - \int_{-h-\Delta h}^{-\Delta h} (p_0 - \rho g\Delta h)dz \tag{15}$$

$$S'_{xx} = A + B + C + D \tag{16}$$

As the linear wave theory, we have the pressure term. Now, integrating this term by the above limit, we obtain

$$A = \frac{\rho_w g}{2}(h+\Delta h)^2 - \frac{\rho_w g H^2}{16} + \frac{\rho_w g H^2 kh}{8\sinh 2kh} \tag{17}$$

At the free surface p is almost equivalent to the static pressure factor beneath the free surface, which is reported by [9] as:

$$p = \rho_w g(\bar{\eta} - z) \tag{18}$$

So, the above eq. (18) simplified as:

$$B = \frac{\rho_w g H^2}{16} \tag{19}$$

We know, the elevation of water surface's is defined as

$$\bar{\eta} = \frac{H}{2}\cos(kx - \sigma t) \tag{20}$$

Again, with the help of Eq. (1), (6) and (20) and taking time average simplification, we obtain

$$C = \frac{\rho_w g H^2}{32\sinh 2kh}\{2kh + c_0 h(1+2k)\} \tag{21}$$

neglecting higher power of

And, using the static pressure, we obtain

$$D = -\frac{\rho_w g}{2}(h+\Delta h)^2 + \rho_w h\Delta h \tag{22}$$

Now, putting the value of *A, B, C* and *D* in Eq. (16) and using Eq. (3), we obtain

$$S'_{xx} = \rho_w g\left(\frac{C_0 h^2}{2-C_0} + \frac{kh}{8\sinh 2kh} + \frac{H^2\{2kh + C_0 h(1+2k)\}}{32\sinh 2kh}\right) \tag{23}$$

which is the radiation stress in terms of air bubble effect. If, there is no air bubble is present then we obtain as [3] radiation stress formula.

2.5 Modified Momentum Balance Equation

The momentum flux is changed due to entrained air bubble, but the bottom pressure is fixed [3]. So that the momentum conservation equation is changed a

$$\frac{d\bar{\eta}}{dx} + \frac{1}{\rho_w g Q}\frac{dS'_{xx}}{dx} - \frac{R}{Q}\frac{dh}{dx} + \frac{S}{Q}\frac{dh}{dx} = 0 \tag{24}$$

where,

$$Q = \bar{\eta} + h - \frac{C_0 h}{2} - \bar{\eta}C_0 \tag{25}$$

$$R = \frac{C_0 h}{3} + \frac{\bar{\eta}C_0}{2} \tag{26}$$

and

$$S = \frac{C_0 h}{2} + \bar{\eta}C_0 \tag{27}$$

3. NUMERICAL PROCEDURE

In the earlier method, most of the model was solved by Finite Difference Method (FDM). But we have used to solve the governing eq. (24) by one dimensional Lax-Wendroff Method, which gives the better results of any other models [14]. Its accuracy up to 2nd order is the best.

3.1 Discretization

To determine wave set-up, we need to solve eq. (24) and the energy balance equation which was described by [14], simultaneously.

Applying the Lax-Wendroff scheme, the difference equation of eq. (24) be as:

$$\bar{\eta}_j^{k+1} = \bar{\eta}_j^k - \frac{\delta}{2\rho_w g Q}\{\acute{S}^k_{xx(j+1)} - \acute{S}^k_{xx(j-1)}\} + \frac{\delta^2}{2\rho_w g Q}\{\acute{S}^k_{xx(j+1)} - 2\acute{S}^k_{xx(j)} + \acute{S}^k_{xx(j-1)}\} - \frac{R}{2Q}(h^k_{j+1} - h^k_{j-1}) + \frac{\delta R}{2Q}(h^k_{j+1} - h^k_j + h^k_{j-1}) - \frac{S}{Q}(h^k_{j+1} - h^k_{j-1}) \tag{28}$$

where, $j = 1,2,3,.....n$, $S'^k_{x\,(j)}$ be the radiation stress including air bubble effect and $\delta = \frac{1}{2\Delta x}$.

In eq. (28), all of the quantities on the right hand side are known, so we can easily calculate the value of $\bar{\eta}_j^{k+1}$.

3.2 Stability Analysis

As in [14], the Von-Neumann stability analysis of the Lax-Wendroff scheme is satisfied the CFL (Courant-Frederic's - Lewy) condition.

So that, the Lax-Wendroff numerical scheme is courant stable for this model.

3.3 Initial Conditions

To calculate the eq. (28), there are two boundary conditions are required: (i) the offshore boundary (ii) the coastal boundary.

For this given situation, the data is required in the breaking zone as the starting zone to the shoreline:

(a) The wave height *H* and still water depth *h* at the close to the shore area.

(b) The bottom profile and wave period *T*.

(c) Moreover, the reference parameters, such as the void fraction C_0 = 0.25 and the free parameter $\beta = 0.8$ is considered for plunging breaker.

(d) C_0 = 0.25 and the free parameter $\beta = 1.17$ are for spilling breaker.

(e) Constant depth considered at the shoreline to avoid the undefined value of wave height as [14].

3.4 Computational Procedure

To calculate the wave set-up, the computation procedure is presented by the following flowchart which is described in Fig. 3:

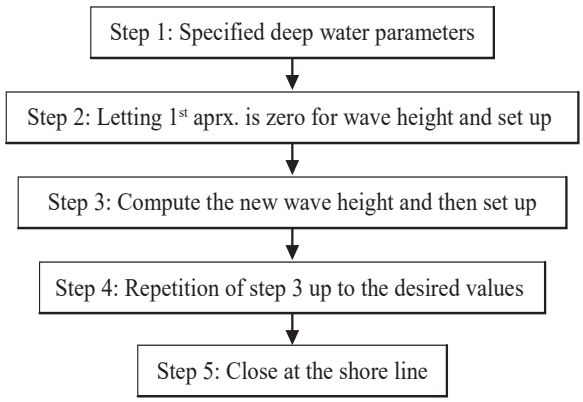

Fig. 3: Stream outline of the computational methodology.

4. RESULTS AND DISCUSSION

The regular waves including air bubble impacts is contrasted with the test results for sloping sea shore with a slope of 1/9.5 given by e [19]. The test was done in a 20 m-long, 0.80 m-wide and 0.60 m-depth wave flume.

The wave period was 1.12 s and 1.80 s for spilling and plunging breakers separately and loaded up with new water to a profundity of 0.40 m. Toward the finish of the wave flume, a wave safeguard was introduced to decrease reflection. Nitty gritty trials were given by [19], so we are not added here. The mathematical outcomes are confirmed with the down to earth information, standardized to their particular breaking esteems. Fig's. 8 and 9 shows the examination of wave setup which is determined by the force balance condition and then depicted by Eq. (24) at H0/L0 = 0.038 and H0/L0 = 0.076 for spilling and plunging breakers individually. As can be seen, the general understanding apparently is genuinely acceptable, albeit a slight variability in Fig. 8, because the data of its appearance in plunging breaker's. Fig's. 4, 5, 6 and 7 are showed that the comparison between present model and various popular model. A comparable variety can likewise be seen in different examinations, for example, [6] in Fig. 6. Two apparent reasons were noted by [6] and [10] for this inconvenience. As in, [1] first noted that after breaking point, no energy is dissipated until the curl touches down and white water appears. The effects of the roller in the breaking wave representation increases the momentum flux and therefore, the two effects may compensate each other mentioned by [6].

The results are showed excellent matched with the other results. The overall results of this developed model is found tremendous in the case of spilling breaking conditions; but, for plunging breaker, the obtain wave setup curve follows the little bit inconsistency at initial stage of start of wave set-up (Fig. 8).

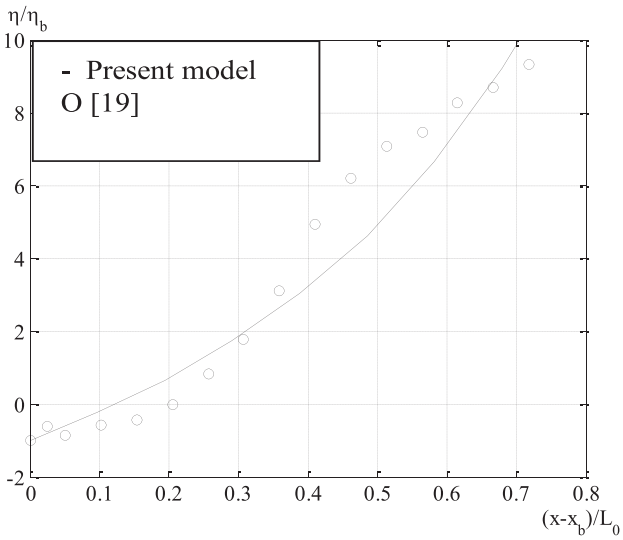

Fig. 4: Comparison of wave setup between present model and [19] for H_0/L_0 =0.062; β =1.5; C_0 = 0.20.

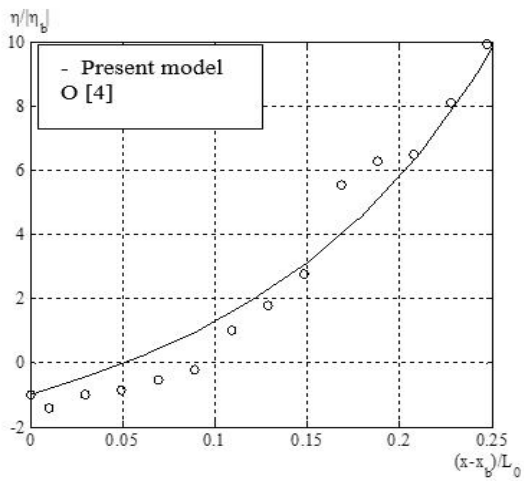

Fig. 5: Comparison of wave setup between present model and [4] for H_0/L_0 = 0.024; β = 0.80; C_0 = 0.20.

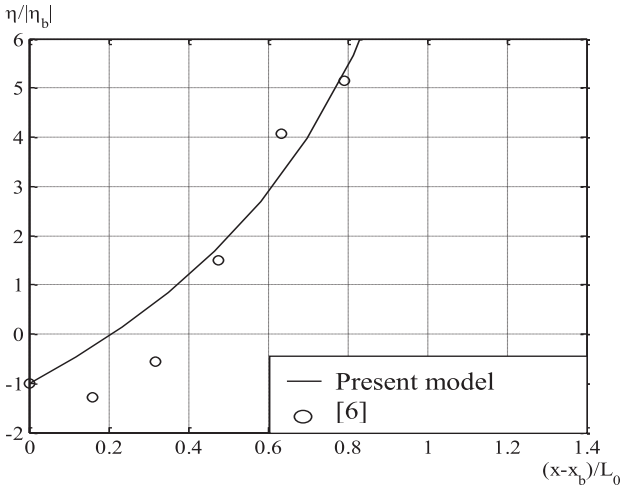

Fig. 6: Comparison of wave setup between present model and [6] for $H_0/L_0 = 0.062$; $\beta = 0.45$; $C_0 = 0.20$.

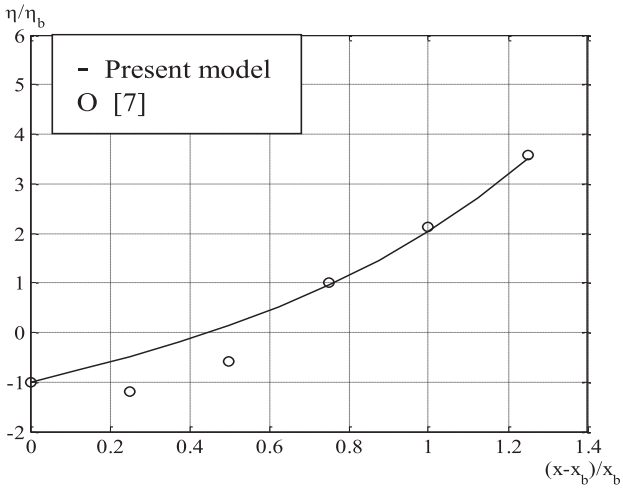

Fig. 7: Comparison of wave setup between present model and [7] for $H_0/L_0 = 0.062$; $\beta = 1.50$; $C_0 = 0.20$.

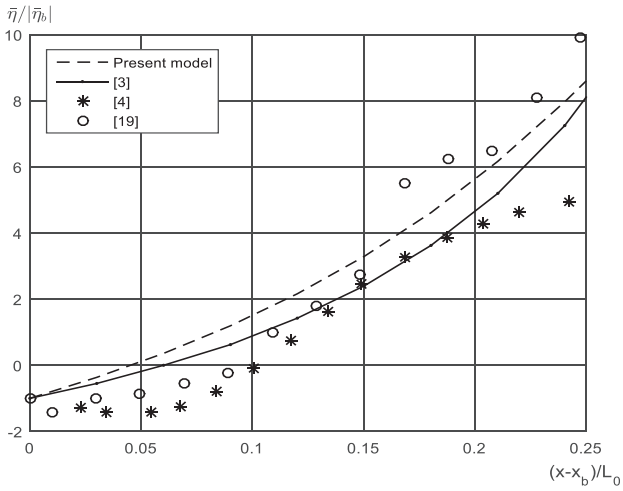

Fig. 8: Comparison of wave setup among various models and experimental data for $H_0/L_0 = 0.038$ (Plunging breakers condition).

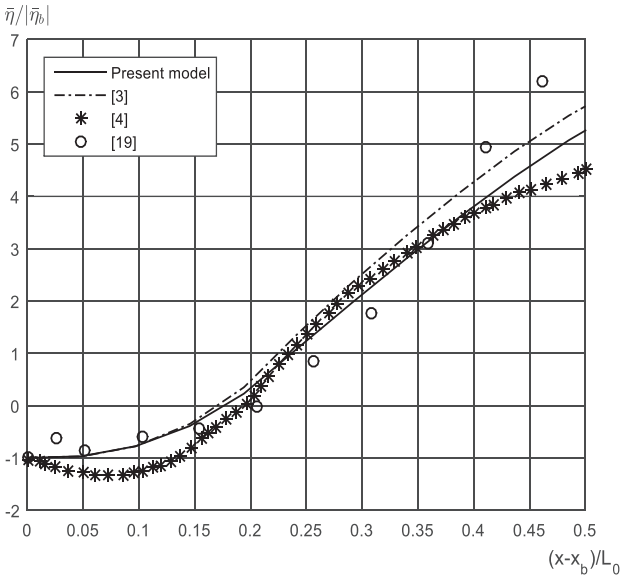

Fig. 9: Comparison of wave setup among present models, different models and experimental data for $H_0/L_0 = 0.076$ (Spilling breaker's condition).

5. CONCLUSION

The radiation stress and the vertical velocity component were developed theoretically considering the air bubble effect. Modified momentum balance equation was solved by Lax-Wendroof scheme and found good agreement with the experimental data and different models in the spilling breaker condition. In the plunging breaking waves little bit inconsistency was found, because the lag between early wave breaking and the initial wave set-up.

REFERENCES

[1] J. C. Strikwerda, Finite Difference Schemes and Partial Differential equation (2nd ed.), Society for Industrial and Applied Mathematics (SIAM), 2004.

[2] R. G. Dean and R. A. Dalrymple, Water wave mechanics for engineers and scientists (2nd ed.), World Scientific, 1990.

[3] A. Hoque, N. Hossain, S. Ali and M. Rahman, "Wave breaking and bubble formation associate energy dissipation and wave setup," Ocean Dynamics, Vol. 69, pp.913-923, 2019.

[4] A. Hoque and S. Aoki, "Wave energy dissipation and wave setup caused by entrained air bubble in plunging wave breaking," Journal of Waterway, Port, Coastal, and Ocean Engineering, Vol. 140, No. 5, pp. 040140201 - 040140209, 2014.

[5] G. Z. Forristall, "On the Statistical Distribution of Wave Heights in a Storm," Journal of Geophysical Research, Vol. 83, No. C5, pp. 2353-2358, 1978.

[6] I. A. Svendsen, "Wave height and set-up in a surf zone," Coastal Engineering, Vol. 8, No. 4, pp. 303-329, 1984.

[7] M. J. F. Stive and H. G. Wind, "A study of radiation stress and set-up in the near-shore region," Coastal Engineering, Vol. 6, No. 1, pp. 1-25, 1982.

[8] M. S. Longuet-Higgins, "On the Statistical Distribution of Wave Heights of Sea Waves," Journal Marine Research., Vol. 11, No. 3, pp. 245-266, 1952.

[9] M. S. Longguet-Higgins and Stewart, "Radiation stresses in water waves; a physical discussion, with applications," Deep Sea Research and Oceanographic Abstracts, Vol. 11, No. 4, pp. 529-562, 1964.

[10] W. R. Dally, R. G. Dean, and R. A. Dalrymple, "Wave height variation across beaches of arbitrary profile," Journal of Geophysical Research, Vol. 90, No. C6, pp. 11917-11927, 1985.

[11] S. A. Thorpe, "On the clouds of bubble formed by breaking wind waves in deep water, and their role in air-sea gas transfer," Philosophical Transactions of the Royal Society of London, Vol. 304, No. 1483, 155– 210, 1982.

[12] D. T. Cox and S. Shin, "Laboratory measurements of void fraction and turbulence in the bore region of surf zone waves," Journal of Engineering Mechanics, Vol. 129, No. 10, pp. 1197– 1205, 2003.

[13] J. Wu, "Bubble in the near-surface ocean: a general description," Journal of Geophysical Research, Vol. 93, No. C1, pp. 587-590, 1988.

[14] M. N. Hossain, M. A. Hoque, M. N. Akhter and M. M. Rahman, "Solution of Linear Water Wave Problems by Lax-Wendroff Scheme", DUET Journal, Vol. 5, No. 2, pp. 55-60, 2019.

[15] A. Fuhrboter, "Air entrainment and energy dissipation in breakers," 12th International Conference on Coastal Engineering, pp. 391-398, 1970.

[16] H. H. Hwung, J. M. Chyan, and Y. C. Chung, "Energy dissipation and air bubble mixing inside surf zone," 23rd International Conference on Coastal Engineering, pp. 308-321, 1992.

[17] J. A. Battjes, and J. P. F. M. Janssen, "Energy loss and set-up due to breaking of random waves," 16th International Conference on Coastal Engineering, pp. 569-587, 1978.

[18] K. Horikawa and C. T. Kuo, "A study on wave transformation inside surf zone," 10th International Conference on Coastal Engineering, pp. 217-233, 1966.

[19] M. A. Hoque and S. Aoki, "Air bubble entrainment by breaking waves and associated energy dissipation," Ph.D. thesis, Toyohashi University of Technology, Japan, Feb. 2002.

[20] P. G. Kasanova, "Numerical methods for the solution of partial differential equations: A review," Institute of Mathematics, UNAM, Rep. 01, 2005.

Pedestrian Behavior and Footpath Service Quality in Hilly Tract Region in Bangladesh

Mohammad Kabir Hossain, Md. Tawkir Ahmed and Md. Rakibul Islam*

Department of Civil Engineering, Dhaka University of Engineering and Technology, Gazipur, Bangladesh

ABSTRACT

Pedestrian level of service is an important parameter to understand the walking condition of footpath. This study evaluates pedestrian behavior and footpath service quality in hilly tracts region in Bangladesh. Analyses show that most of the pedestrian (about 35%) would like to walk for 15-20 minutes. Average walking speed of pedestrian is highest for single man and lowest for man and women with good interaction. Pedestrian level of service is highest in the Marine Drive road and lowest in the Teknaf Bus stand road. Existing footpath facilities is also poor in the study region. Findings of this study will help the city planners and engineers in making future polices to improve pedestrian facilities.

***Keywords*:** Footpath, Pedestrian, Teknaf, Hilly Tract Region.

1. INTRODUCTION

Footpath is an important part of complete road systems. It is considered as the important mode of transport in the developed countries [1]. Footpath can be used for different types of activities like cycling, animal movement, recreation activities etc. However, developing country like Bangladesh the term footpath is not well defined. Most of the footpaths are not properly designed and well-connected and this causes destruction of pedestrian flow in Bangladesh [2]. Insufficient number of footpaths in this country causes pedestrian to use main road that causes series of accidents in road [3]. Measures taken to ameliorate the issue has failed to perform effectively [2-3].

Reviewing existing literatures suggest that lots of importance were given on pedestrian behavior and footpath service quality. Daniel et al. (2016) studied pedestrian footpath level of service (FOOT-LOS) and found several attributes like mobility, comfort and safety are affecting pedestrian service quality. They developed FOOT-LOS (pedestrian footpath level of service) model to facilitate the LOS measurement which depend on the footpath width (meter), road width (meter), surface damage (% of area), number of obstructions (number per 100 meter), pedestrian flow (pedestrians/minute/meter), and traffic volume (vehicles/hour) [4].

Furthermore, Kelly et al. (2011) studied on pedestrian walkability environment using three statistical method. They found pavement cleanliness, safe crossing places, connectivity and security, and found the walking experiences are affected by cumulative impact of multiple interactions (both positive and negative) as people walk in the pedestrian environment [5]. Ahmed and Islam (2020) accessed roadside walkway environment in Gazipur city.

They determine footpath LOS based on HCM (Highway Capacity Manual). They found several unsocial activities (Hijacking, Pick-pocketing and Bad comments) occurs specially for women and vendor activity reduces the width of footpath. It causes pedestrian to use road which causes road accident [6]. Furthermore, some studies give importance on LOS model development. Bivina et al. (2018) developed a Structural Equation Model (SEM) to access pedestrian service quality [7]. They found that police patrolling, street lighting, cleaner sidewalks, sidewalk obstructions, and sidewalk surface are affecting footpath service quality.

Back to country very few researches have been paid attention on pedestrian and footpath issues. Ahmed, Islam and Adetayo (2020) studied footpath service quality in a major industrial zone in Bangladesh, using both qualitative and quantitative approaches. They consider the factors gender distribution during day and night, Age distribution of Responded, Gender wise of purpose of using footpath, Footpath use in terms of purpose, Hourly flow of pedestrian, and Personal Insecurity level of using footpath for determining footpath service quality. They estimated people opinion score about footpath is 2.66 (out of 5). Which is unsatisfactory and undesirable for industrialized area [2]. Bhuiya et al. (2020) evaluated pedestrian level of service of selected footpath segments in Dhaka city.

*Corresponding author's email: rakibul10@duet.ac.bd

They found footpath level of service depends on path width, pedestrian volume, crossing facilities, availability of buffer, distance from vehicular traffic, surface quality, convenience, walkway environment, street light [8]. Siddique (2014) studied walkways in Dhaka City and proposed that eight factors had direct impact on the walkway level of service. The factors are width, surface condition, obstruction, roadway crossing facilities, buffer zone between footpath and roadway, presence of bicycle and motorcycle over footpath, walkway lighting, and queue of trees along the footpath [9].

Unfortunately, pedestrian and footpath service quality are still unknown in Teknaf. This encourages the authors to explore the actual condition of the pedestrian and footpaths facilities in Teknaf. It will help to develop a concession point to ameliorate the existing condition.

2. STUDY AREA

Teknaf is considered as a hilly tract region in Bangladesh. It is situated at Cox's Bazar District in Chittagong (Fig.1). The city shares it borders with Myanmar, which coordinate is 20.8667°N and 92.3000°E. Total 23,675 households are lived in the 388.68 km^2 area [10]. Teknaf had a population of 152,557 where males 51.81% and females 48.19%. Teknaf has 6 Unions, 13 Mauzas, and 133 villages. The six unions are Teknaf Union, Hnila Union, Baharchhara Union, Sabrang Union, Whykong Union, St. Martin Dip [11]. The area is selected based on the geographical importance and to explore the area for the first time (Fig.1). Though, Teknaf is enriched with tourist and different businesses but, no study has been done of pedestrian and footpath facilities. Those phenomena encouraged the authors to explore the area and find out different problems with its solution regarding pedestrian and footpath. The study will be a bench mark for pedestrian and footpath facilities development in Teknaf city [10-11].

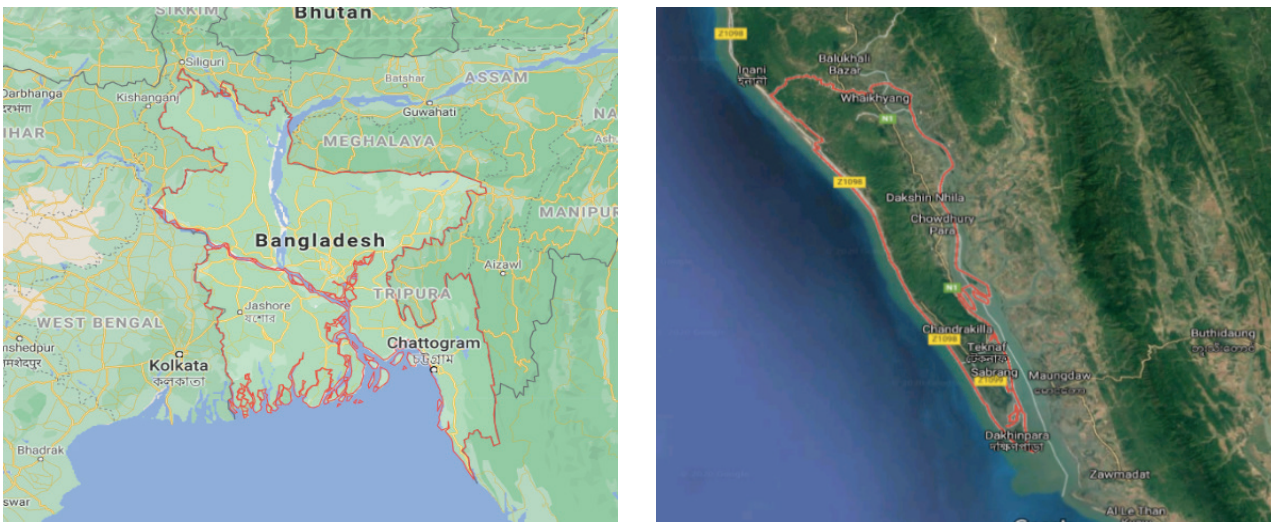

Fig. 1: Geographical view of Teknaf

3. METHODOLOGY

The methodology of this study is designed based on previous literature (Fig.2). The frame is started based on defining objectives. Reviewing previous literature helps to identify several factors which are related with our research topic. After that important locations were selected based on geographical importance. Preliminary concept of the study area was gained from reconnaissance Survey. Data was collected in the selected point where pedestrian movements are significant. MS Excel software has been used to analyze the survey data. Results are presented in a precise way in the results section. Finally, the frame end with the outcome of this study. Recommendation has been made based on the outcome of the study (Fig.2).

Pedestrian survey was carried out in three selected routes (Route 1: Teknaf-Cox's Bazar Road, Route 2: Old Marine Drive Road, Route 3: New Marine Drive Road) between 02/09/2020 to 03/09/2020 (Fig.3). Those routes are selected based on the geographic importance. However, Maximum number of pedestrian pass through those three

points (Location 1: Teknaf Bus Stand Point, Location 2: Parjatan Bazar Point, Location 3: Teknaf Beach Point) (Fig.4).

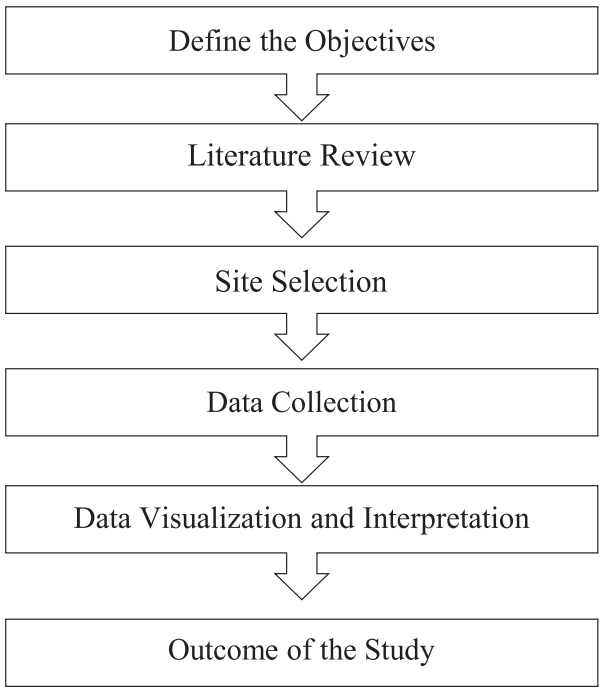

Fig. 2: Methodology of the study

Data were collected in three steps, 1. Pedestrian number was counted in the three important points using counting machine and video camera in a particular segment (5m), 2. Pedestrian speed was counted using speed gun in the three important places, 3. Public opinion about footpath service quality attributes were collected along with their demographic information (Fig.4).

(a) Study routes of Tenkaf

(b) Pictorial view of route 1

(c) Pictorial view of route 2

(d) Pictorial view of route 3

Fig. 3: Geographical view of study routes

(a) Survey at route 1

(b) Survey at route 2

(c) Survey at route 3

(d) Footpath measurement survey

Fig. 4: Pictorial view of pedestrian and footpath condition survey

3.1 Pedestrian Walking Speed

For calculation of average walking speed, a strip of 5m was considered and then the time of passing this strip for each category pedestrian was recorded. Average walking speed was calculated using the following formula:

$$V = S/t \quad (1)$$

Where,

S= Travel distance
V=Speed of the pedestrian
t =Time required for travel distance

3.2 Pedestrian Level of Service

Level of Service (LOS) for pedestrian is an important tools to evaluate overall measure of walkway conditions. LOS is directly related with mobility, comfort and safety, and reflecting pedestrian understand about different footpath facilities. Table I describes the HCM (Highway Capacity Manual) average flow criteria for assessing the LOS of pedestrian [12]. LOS A is considered as good condition and LOS F is considered as worse (Table I).

Table I: HCM average flow criteria for assessing the LOS of pedestrian.

LOS	Pedestrian Space (ft^2/Ped)	Pedestrian Flow Rate (Ped/min/ft)
A	> 60	< 5
B	>40-60	> 5-7
C	>24-40	> 7-10
D	>15-24	> 10-15
E	> 8-15	>15-23
F	< 8	Variable

4. RESULTS AND DISCUSSION

In Table II, shows the demographic characteristics of pedestrians where, in terms of gender, male is 69 % on the other hand female is 31%. It indicates, males are used footpath on regular basis compare with females. In terms of age, adult is the dominant one which is 55%. It means that, child and older age group are less user of footpath because they faced difficulties in using footpath.

Table II: Demographic characteristics of pedestrian

	Type	%
Gender	Male	69
	Female	31
Age(years)	Child (0-15)	36
	Adult (16-50)	55
	Older (50+)	9

4.1 Average Walking Speed of the Pedestrian

Fig. 5 shows that average walking speed is high for single male and its value is 1.18 m/s. Second highest speed has been observed 1.02 m/s for double male. Lowest Average speed of walking has been observed 0.85 m/s for Male and Female with good interaction (Fig. 5).

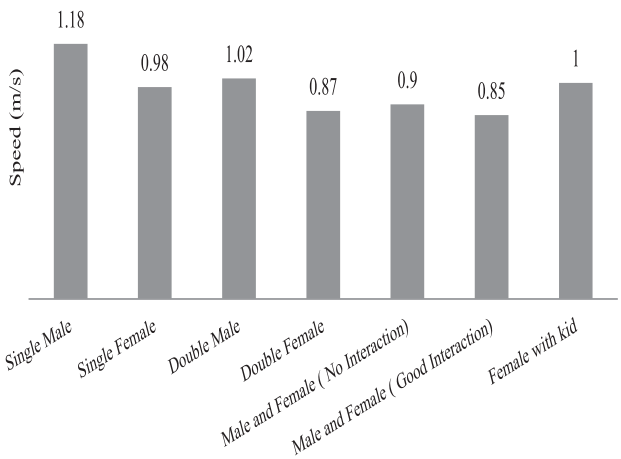

Fig. 5: Average pedestrian walking speed (m/s)

4.2 Average Walking time of the Pedestrian

Analysis shows that most of the respondents (about 35%) would like to walk for a period of 15-20 minutes. About 5% of the respondents would like to walk more than 30 minutes. About 13% of people would like to walk for a period less than 10 minutes (Fig. 6).

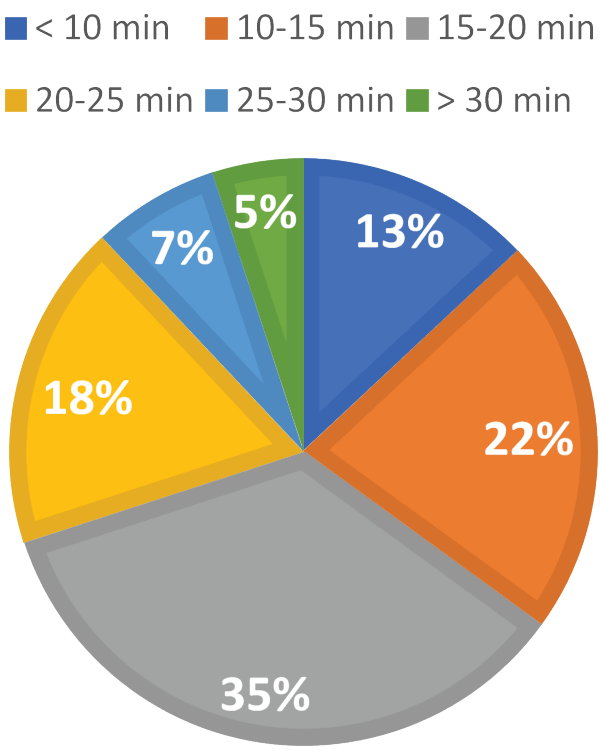

Fig. 6: Average Walking Time of Pedestrians (min)

4.3 Pedestrian Level of Services

4.3.1 Teknaf bus stand point

The analysis shows that the pedestrian level of services in A category at 7 am-8 am at this point. In the morning pedestrian flow rate is higher at 9 am-10 am and its value is 14 ped/min/ft because people of different professions use this time to reach their destination. In the afternoon pedestrian flow rate is more at 1 pm-2 pm (Fig.7). The average pedestrian flow rate is high in evening, and 6 pm-7 pm time contains the maximum flow rate with a value of 16 ped/min/ft. Working people go home and most of the non-working people go outside of the home at evening that's why the pedestrian flow rate is more at this time (Table III).

Table III: Level of services of pedestrian at Teknaf Bus Stand Point

Time	Pedestrian Flow Rate (ped/min/ft)	LOS
7am-8am	2	A
8am-9am	6	B
9am-10am	14	D
10am-11am	8	C
11am-12pm	6	B
12pm-1pm	11	D
1pm-2pm	13	D
2pm-3pm	9	C
3pm-4pm	5	B
4pm-5pm	9	C
5pm-6pm	12	D
6pm-7pm	16	E

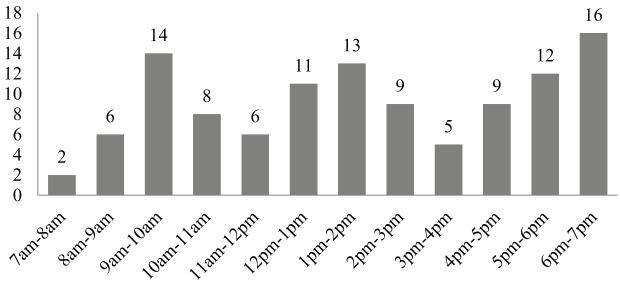

Fig. 7: Variation of pedestrian flow rate (ped/min/ft) at Teknaf Bus Stand Point

4.3.2 Teknaf beach point

The average level of services (LOS) of pedestrian in A category in morning in Teknaf beach point [13-14]. The pedestrian flow rate is highest at 5 pm-6 pm and its value is 10 ped/min/ft (Fig.8). The average level of service accomplishes C category in the evening because people of all classes come to this point for their refreshment in the evening (Table IV).

Table IV: Level of Services of Pedestrian at Teknaf Beach Point

Time	Pedestrian Flow Rate (ped/min/ft)	LOS
7am-8am	1	A
8am-9am	2	A
9am-10am	5	B
10am-11am	3	A
11am-12pm	2	A
12pm-1pm	4	A
1pm-2pm	3	A
2pm-3pm	1	A
3pm-4pm	6	B
4pm-5pm	9	C
5pm-6pm	10	D
6pm-7pm	8	C

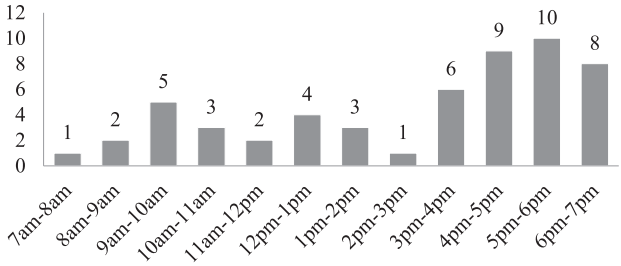

Fig. 8: Variation of pedestrian flow rate (ped/min/ft) at Teknaf Beach Point

4.3.3 Parjatan bazar point

Table V and Fig. 9 shows pedestrian level of service at Parjatan Bazar point. Results show, pedestrian flow rate is less in very morning time (Table V). Highest flow rate is 11 ped/min/ft at 1pm-2pm and 5pm-6pm (Fig. 9).

Table V: Level of Services of Pedestrian at Parjatan Bazar Point

Time	Pedestrian Flow Rate (ped/min/ft)	LOS
7am-8am	1	A
8am-9am	3	A
9am-10am	6	B
10am-11am	8	C
11am-12pm	5	B
12pm-1pm	9	C
1pm-2pm	11	D
2pm-3pm	6	B
3pm-4pm	4	A
4pm-5pm	5	B
5pm-6pm	11	D
6pm-7pm	8	C

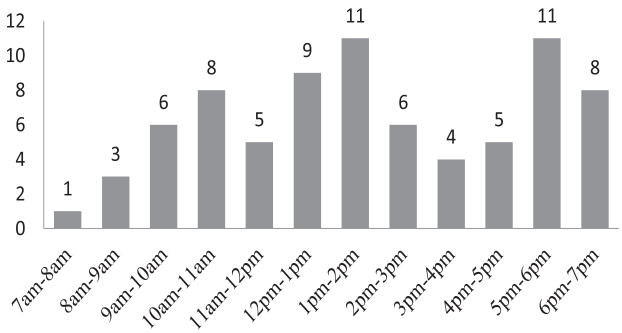

Fig. 9: Variation of pedestrian flow rate (ped/min/ft) at Parjatan Bazar Point

4.4 Footpath Facilities

Fig. 10 shows overall footpath condition from questioner survey. The footpath condition is much worse than road condition. Most of the cases the road has no footpath facilities. 71.14% respondents response that the footpath facilities are in poor condition. Field investigation revealed that most of the road has no footpath and people use the road as footpath which reduces the effective road width and causes severe road accident (Fig. 10).

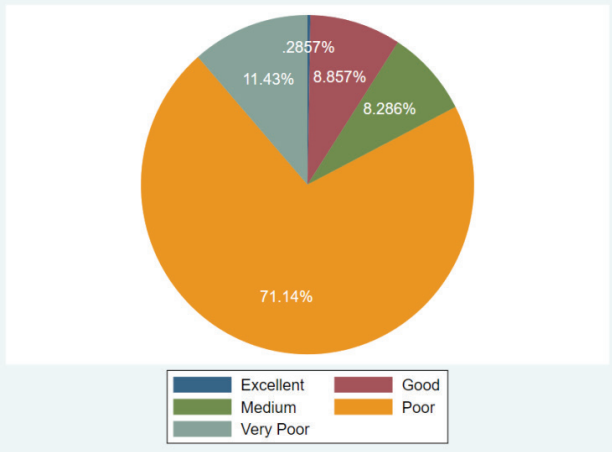

Fig. 10: Footpath overall condition

Fig. 11 shows the 16 footpath service quality attributes. The attributes were collected based on the Likert scale 1 to 5 rating, where 1 means very poor, 2 means poor, 3 means medium, 4 means good, and 5 means excellent. Movement of bicycles, bicycles and security for sexual harassment are good factors and surface condition, height of sidewalks, presence of barrier, and lighting facilities are in very poor condition. It means that, footpath several factors should be improved on importance basis.

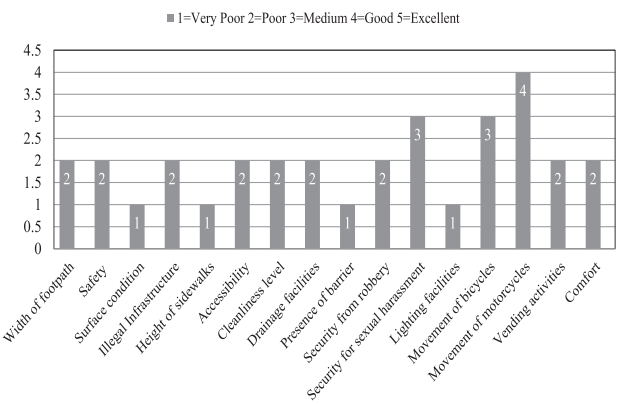

Fig. 11: Footpath attributes survey

5. CONCLUSION

Footpath is a major component of a complete road system. Service quality of any road mostly related with footpath facilities and pedestrian behavior. Footpath space can be utilized by rebalancing illegal activities on footpath space. In case of hilly region footpath facilities should be adequate because of narrow road pattern to avoid road accidents. The aim of this paper to evaluate pedestrian behavior and quality assessment of footpath in hilly region in Bangladesh. From result, it is seen that about 35% pedestrians walk about 15-20 minutes and only 5% pedestrians walk more than 30 minutes. Average walking speed is high for single male and its value is 1.18m/s. Male and female with good interaction contains less average walking speed with value of 0.85m/s. Pedestrians flow rate is high in Teknaf Bus stand point with average pedestrian level of service (PLOS) in D category and less in Teknaf Beach point with average pedestrian level of service in B category. Hence, it is seen that PLOS is satisfactory in all three roads of Tekanf, this scenario mainly due to less density of population at the area. Teknaf Bus stand road is the main route to travel for all types of vehicles and pedestrians from others parts of the country, so pedestrians flow rate is high in this road. Analysis of respondent's opinion most of the people responses that existing conditions of footpath is worst.

From the study outcomes, the following point can be put forward to improve the present footpath facilities. It will help to fulfill the future demand: 1. Surface condition of footpath need to improve. 2. Height of footpath should be separated from main road. 3. Presence of barrier should be removed on footpath (vendor activities, pothole, construction materials etc.). 4. Sufficient lighting for footpath should be provided especially for night condition.

REFERENCES

[1] M. Abdel-Aty, A. Pande, C. Lee, V. Gayah, and C. D. Santos, "Crash Risk Assessment Using Intelligent Transportation Systems Data and Real-Time Intervention Strategies to Improve Safety on Freeways," Journal of Intelligent Transportation Systems, 11, 107 – 120, 2007.

[2] M. T. Ahmed, M. R. Islam, and A. Adetayo, "Service Quality Assessment of Footpath in a Major Industrial Zone of a Developing Country: A Case Study of GAZIPUR City, Bangladesh," J. Transp. Eng. Its Appl., vol. 5, no. 1, pp. 1–20, 2020.

[3] M. K. Hossain, M. T. Ahmed, and M. R. Islam, "Vehicle Characteristics and Roadway Level of Service of Industrial Zone : A Typical Example of Gazipur Chowrasta Intersection," DUET J., vol. 5, no. 2, pp. 61–73, 2019.

[4] B. D. Daniel, S. N. Mohamad Nor, M. Md Rohani, J. Prasetijo, M. Y. Aman, and K. Ambak, "Pedestrian Footpath Level of Service (FOOT-LOS) Model for Johor Bahru," MATEC Web Conf., vol. 47, p. 3006, Apr. 2016.

[5] C. E. Kelly, M. R. Tight, F. C. Hodgson, and M. W. Page, "A comparison of three methods for assessing the walkability of the pedestrian environment," J. Transp. Geogr., vol. 19, no. 6, pp. 1500–1508, Nov. 2011.

[6] M. T. Ahmed, and M. R. Islam, "Qualitative Assessment of the Roadside Walkway Environment for an Industrialized Zone: An Empirical Example of Gazipur City Corporation, Bangladesh," 5th International Conference on Advances in Civil Engineering (ICACE-2020), 2020.

[7] G. R. Bivina and M. Parida, "Modelling Perceived Pedestrian Level of Service of Sidewalks: A Structural Equation Approach," Transport, Vol. 34, No. 3, pp. 339–350, May 2019.

[8] M. R. Bhuiya, H. Mohiuddin, S. H. Patwary, and A. Tasneem, "Evaluation of Pedestrian Level of Service of Selected Footpath Segments of Dhaka City using Multi-criteria Decision Making Approach," vol. 20, no. 1, 2020.

[9] A. Siddique, "Determination of a Suitable Level of Service Method To Measure Service Quality of Pedestrian Walkways in Dhaka City," Post graduate dissertions (Thesis) of Department of Civiel Engineering (CE), BUET, 2014.

[10] M. Tani and M. A. Rahman, "Deforestation in the Teknaf Peninsula of Bangladesh," Singapore: Springer Singapore, 2018.

[11] M. Paul, K. Alam and M. S. Islam, "Behind Successful and Uuseccessful Overseas Migration : What Matters ? A Case Study of Bangladesh," IIASS, Vol. 12, No. 1, January, 2019.

[12] HCM, Highway Capacity Manual 2010. Washington DC: Division of Engineering and Industrial Research National Academy of Sciences-National Research Council. 2010.

[13] M. K. Hossain, M. T. Ahmed, and M. R. Islam, "Traffic Characteristics in Hilly Tract Region of Bangladesh," Journal of Transportation Systems, vol. 6, no. 1, 2021.

[14] M. S. B. Siraj, M. K. Hossain, M. T. Ahmed, and M. R. Islam, "Pedestrian Flow Characteristics Adjacent to Different Educational Institutions of Chittagong City, Bangladesh," Journal of Transportation Systems, vol. 6, no. 1, 2021.

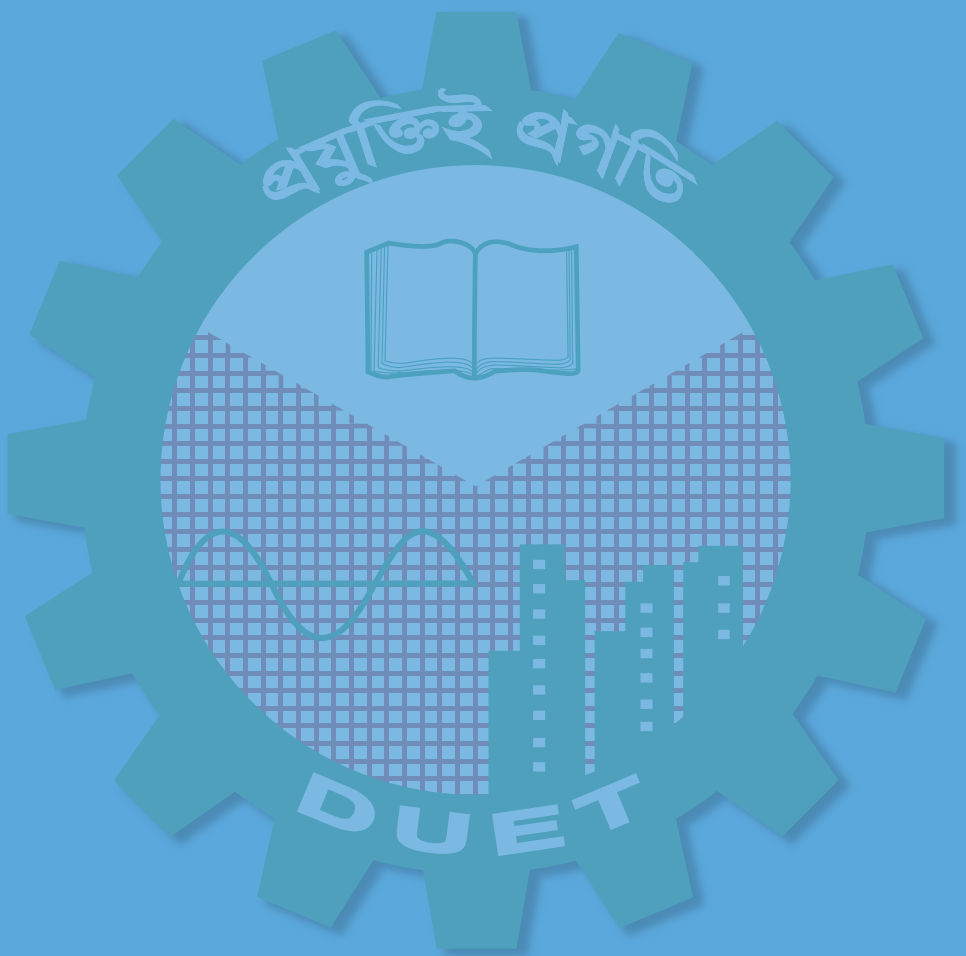

Printed by: Sowrov Media Products, Phone : 01718-419001